POLYTECHNIC OF TURIN

Master's Degree in Aerospace Engineering



Master's Degree Thesis

A Low-fidelity Framework for Propeller Noise Prediction

Supervisors

Candidate

Prof. Francesco AVALLONE

Giuseppe Riccardo FORNARI

Dott. Francesco BELLELLI

Dott. Marco PICILLO

Dott. Alberto ARTONI

2024/2025

I dedicate this work to my girlfriend, Greta,
to my mother, Ilenia,
to my father, Carmelo,
to my brother, Francesco,
and to the rest of my family.

Abstract

Due to the tightening of the regulations on emitted sound and pollution in civil aviation, new aircraft concepts were recently investigated. Well-known examples are electric Vertical Take-off and Landing (eVTOL), aircraft equipped with distributed propulsion systems, and drones. The increasing complexity of this new generation of aircraft makes the accurate prediction of the aerodynamics and aeroacoustics performance a more challenging task. Existing high-fidelity tools excel at predicting such performance, but they require a high computational cost and time. Moreover, the current low-fidelity tools often show limitations when applied to complex configurations such as the distributed propulsion systems. Then, the scientific community is looking for new tools able to support every step of the design process of the more quieter and sustainable aircraft.

In this work, the numerical framework based on the Vortex Particle Method (VPM), FLOWUnsteady, was coupled with an in-house aeroacoustics solver using the *Ffowcs Williams-Hawkings analogy* (FWH) for tonal noise and the *Amiet approach* fed with Wall Pressure Fluctuation functions for broadband noise. The solver was validated against high-fidelity numerical and experimental data, showing high accuracy with a low computational cost. Finally, the framework was used to investigate the interaction effect between adjacent propellers in different configurations.

The aerodynamic solver exhibits high agreement with high-fidelity numerical and experimental data across a wide range of advance ratios for all configurations considered. The aeroacoustic solver accurately predicts the first Blade Passing Frequency (BPF) for both isolated and distributed configurations with a low computational cost. The accuracy decreases for observer angles in upstream and downstream directions, but remains comparable to the high-fidelity data. Additionally, the distributed propulsion effects on the tonal noise and trailing edge noise were investigated.

This work shows that FLOWUnsteady, coupled with the in-house aeroacoustic solver, provides a valid alternative to the conventional low-, mid-, and high-fidelity

methods, achieving a high accuracy to computational cost ratio. In addition, the work shows that configurations with high aerodynamic interactions increase both tonal and broadband noise in the far field, highlighting the importance of using solvers able to capture unsteady aerodynamics from early stages of the design process.

Acknowledgements

I would like to express my sincere gratitude to Professor Francesco Avallone for his constant support and invaluable guidance throughout the preparation of this thesis. I am particularly grateful for his role not only as a supervisor but also as a mentor, providing insights and lessons that significantly contributed to my personal and professional growth.

I would also like to extend my sincere thanks to my co-supervisors, Francesco Bellelli, Marco Piccillo, and Alberto Artoni, for their collaboration, advice, and continuous support, which made the research process more stimulating, productive, and enjoyable.

I wish to acknowledge my friends and colleagues, some of whom I have known even before my undergraduate studies, for their presence, encouragement, and collaboration, which were fundamental in achieving this milestone. Thanks to them, I was able to broaden my knowledge and enrich my university experience, both academically and personally.

A heartfelt thanks goes to my parents, my brother, and the rest of my family for always encouraging, supporting, and motivating me in pursuing my goals. Their constant support was crucial in allowing me to approach this academic journey with confidence and determination.

Finally, I would like to express my special gratitude to my partner Greta, who has been by my side since the beginning of my undergraduate studies. Her presence, patience, and unwavering support have been a source of strength and balance. Every idea, project, and achievement has been enriched by her involvement and encouragement, making even the most demanding moments more manageable.

Table of Contents

Li	st of	Table	es .	VIII
Li	st of	Figur	res	IX
1	Inti	roduct	ion	1
	1.1	Conte	ext and Motivation	1
	1.2	Objec	etive of the Thesis	3
	1.3	Metho	odology Approach	3
	1.4	Outlin	ne of the Thesis	4
2	Bas	sic Pri	nciples of the Propeller Aerodynamics	6
	2.1	Prope	eller Performance Parameters	6
	2.2	Mathe	ematical Models For Propellers	9
		2.2.1	Actuator Disk	10
		2.2.2	Blade Element Theory	12
		2.2.3	Blade Element Momentum Theory	14
		2.2.4	Reynolds-Avaraged Navier-Stokes	16
		2.2.5	Large Eddy Simulation	16
3	The	eoretic	al Background for FLOWUnsteady	18
	3.1	FLOV	$ ext{VUnsteady} \dots \dots \dots \dots \dots \dots \dots \dots$	19
		3.1.1	Reformulated Vortex Particle Method	19
		3.1.2	Actuator Line Model - Rotor Model	22
		3.1.3	Actuator Surface Model - Wing Model	25
		3.1.4	Framework Execution Logic	27
4	Phy	sics a	nd Modeling of the Propeller Noise	30
	4.1	Physic	cs of Sound	30
		4.1.1	Ffowcs-Williams and Hawkings	32
		4.1.2	Mechanisms of Noise Generation in Rotors	33
	4.2	Aeroa	coustic Framework	

		4.2.1	Tonal Noise	6
		4.2.2	Broadband Noise	9
5	Vali			4
	5.1	Simula	tions Setup	4
	5.2	Isolate	ed Propeller	6
		5.2.1	Aerodynamic Analysis	6
		5.2.2	Aeroacoustics Analysis	1
	5.3	Distrib	outed Propellers	6
		5.3.1	Convergence Analysis	6
		5.3.2	Aerodynamic Analysis	6
		5.3.3	v v	3
6	Con	clusio	a and Future Works 7	0
	6.1	Conclu	ısion	0
	6.2	Future	e Work	1
\mathbf{A}	Wal	l Press	sure Function 7	2
	A.1	Goody	7	2
	A.2	Rozen	berg	4
	A.3			5
	A.4	Catlet	t	6
	A.5			7
	A.6	Lee .		8
В	Rad	liation	Integral 7	9
	B.1	Terms	of Radiation Integral	9
		B.1.1		0
		B.1.2	Subcritical gust	1
Bi	bliog	graphy	8	2

List of Tables

5.1	Number of revolutions required to reach convergence with	
	a relative tolerance of 10^{-5}	47
5.2	Solver parameters for advance ratio analysis	47
5.3	Absolute maximum errors for BEMT and FLOWUnsteady	
	solvers	47
5.4	Solver parameters for detailed analysis	49
5.5	Peak thrust distribution values and their corresponding	
	radial positions.	50
5.6	Number of revolutions required to reach convergence with	
	a relative tolerance of $3 \cdot 10^{-5}$	58
5.7	Solver parameters for advance ratio analysis of the dis-	
	tributed configuration	58
5.8	Solver parameters for advance ratio analysis of the dis-	
	tributed configuration.	58
A.1	Parameters of the Goody Model	73
A.2	Parameters of the Rozenberg Model	74
A.3	Parameters of the Kamruzzaman Model	75
A.4	Parameters of the Catlett Model.	76
A.5	Parameters of the Hu Model	77
A 6	Parameters of the Lee Model	78

List of Figures

1.1	Vahana eVTOL aircraft from Airbus. Image taken from [4].	2
1.2	TUD-XPROP-S from Delft University of Technology. Image	
	taken from [10]	4
2.1	Thrust Coefficient C_T versus advance ratio J of the XPROP	
	geometry. Experimental data from Reference [11]	8
2.2	Torque Coefficients C_Q versus advance ratio J of the XPROP	
	geometry. Experimental data from Reference [11]	8
2.3	Propulsive efficiency η versus advance ratio J of the XPROP	
	geometry. Experimental data from Reference [11]	9
2.4	Actuator disk scheme	10
2.5	Extended actuator disk scheme.	12
2.6	Element of the BEM	13
2.7	Scheme describing the forces and the velocities exerted on	
	a blade element in the Blade Element Theory.	14
2.8	Scheme describing the forces and the velocities exerted on	
	a blade element in the Blade Element Momentum Theory.	15
3.1	Block scheme of immersed vorticity	23
3.2	Rotor's particles used in ALM. Figure extracted from ref-	
	erence [21]	24
3.3	Block scheme of the Actuator Line Model	25
3.4	Scheme of a wing element of a swept wing in the ASM.	
	Image taken from [8]	26
3.5	Block scheme showing the execution logic of FLOWUn- steady. The figure shows the main steps linked in chrono- logical order by arrows. The runtime_function() are rep- resented by the circular path. Exemplified version of the	
	block scheme of the official documentation.	29

4.1	Instantaneous view of the particles and the pressure variations. Figure extracted by Reference [22]	31
4.2	Example of a tonal source signal. Extracted from Reference	
4.3	[24]	34
	Reference [24]	35
4.4	Coordinate system [23]	37
4.5	Scheme of blade planform [23]	38
4.6	Schematic of trialing-edge noise generation. Figure extracted by Reference [27]	40
4.7	Coordinate system of the Amiet Approach for propellers	41
5.1	Geometry of the isolated propeller TUD-XPROP-S	45
5.2	Distributed configuration. The dashed line indicates the wake survey plane.	46
5.3	 (a) Convergence of the three performance parameters. (b) FLOWUnsteady, BEMT and experimental thrust setting at different advance ratios. (c) FLOWUnsteady, BEMT and experimental torque coefficient at different advance ratios. (d) FLOWUnsteady, BEMT and experimental propulsive 	
	efficiency at different advance ratios	48
5.4	Blade Loading comparison of the three solvers with both FLOWUnsteady tripped and no-tripped solution	49
5.5	(a) Phase-locked velocity magnitude in the survey plane of the FLOWUnsteady tripped simulation. (b) Comparison of the normalized axial velocity of the FLOWUnsteady	•
F 0	tripped, no.tripped solution and the VLES solution.	50
5.6	SPL directivity of the first BPF of the isolated rotor on XZ	52
5.7	plane	32
	the tonal signal of the isolated propeller in the rotation axis.	53
5.8	Broadband analyses at different WPF functions for the isolated propeller.	54
5.9	Predicted sprectrum for the isolated propeller	55
5.10	(a)Convergence of the thrust setting as a function of the number of blade elements. (b) Convergence of the thrust setting as a function of the number of shed particles.(c) Convergence of the thrust setting as a function of the	E 77
	number of time steps	57

5.11	(a) Thrust setting comparison between the isolated pro-	
	peller and the middle one in the distributed configuration.	
	(b) Torque coefficient comparison between the isolated pro-	
	peller and the middle one in the distributed configura-	
	tion.(c) Propulsive efficiency setting comparison between	
	the isolated propeller and the middle one in the distributed	
	configuration.	59
5.12	Comparison of the time history of the thrust of each propeller.	60
5.13	Phase-locked thrust setting difference between propellers	
	of the distributed configuration and the isolated propeller.	
	Comparison with result in Reference [9],	61
5.14	Vortex structure of the middle propeller of the distributed	
	configuration.	62
5.15	(a) Comparison of the normalized axial velocity with the	
	VLES results in Reference [9] and the isolated case. (b)	
	Averaged magnitude velocity in a plane 1.2R downstream	
	from the propeller	63
5.16	Directivity of the first BPF of the middle rotor.	64
5.17	(a) Power Spectral Density of the tonal signal of the middle	
	propeller in the rotor plane. (b) Power Spectral Density of	
	the tonal signal of the middle propeller in the rotation axis.	65
5.18	Broadband analyses at different WPF functions for the	
	middle propeller of the distributed configuration with an	
	observer placed in the rotation axis	66
5.19	Predicted sprectrum for the middle propeller of the dis-	
	tributed configuration with an observer placed on the rota-	
	tion axis	66
5.20	(a) Acoustic pressure on the rotor plane. (b) Acoustic pres-	
	sure fluctuation on the rotor plane. (c) Acoustic pressure	
	on the rotation axis. (d) Acoustic pressure fluctuation on	
	the rotation axis	67
5.21	Comparison of the trailing edge noise emission on the rota-	
	tion axis	68
5.22	Comparison of the trailing edge noise emission on the rota-	
	tion axis with other WPF functions. Red lines for Middle	
	propeller and blue lines for the isolated one.	69

Chapter 1

Introduction

1.1 Context and Motivation

The civilian aviation sector has recently begun to undergo a radical transformation aimed at achieving high environmental sustainability. As outlined by the Advisory Council for Aviation Research and Innovation in Europe (ACARE), the main objective is climate neutrality by 2050. In this context, noise emissions have assumed a role of primary importance, no longer considered a secondary comfort factor, but a fundamental design parameter directly linked to the public acceptance of the aviation sector by citizens living near airports [1].

To reduce environmental pollution, the aviation industry is moving toward Urban Air Mobility (UAM). A new class of aircraft, such as drones and Electric Vertical Take-Off and Landing (eVTOL) vehicles, represents the main actors in this vision. Although these technologies are promising for the future of aviation due to their low environmental impact, being powered by electric motors and offering high efficiency, they generate significant noise that can disturb urban populations. Therefore, their use for applications such as package delivery, surveillance, or passenger transport remains limited [2].

One of the most adopted solutions to reduce both climate and noise impacts is represented by Distributed Electric Propulsion systems (DEP). The aircraft equipped with DEP shows various advantages in terms of propulsive and aerodynamic efficiency as well as a potential reduction in the noise emitted thanks to the decoupling between the power generation system and the propulsion system [3].

However, the introduction of DEPs leads to the emergence of totally new and not fully understood aerodynamic interactions recently studied in [5]. The prediction



Figure 1.1: Vahana eVTOL aircraft from Airbus. Image taken from [4].

of these phenomena right from the preliminary design phase is essential to achieve the 65% reduction in emitted noise outlined by ACARE's Fly the Green Deal.

There are many different fidelity numerical methods used to predict rotor performance, but only recently has their ability to predict aerodynamic interactions in DEP configurations been investigated. Low-fidelity methods, such as Blade Element Momentum Theory (BEMT) and Lifting Line Theory (LL), have demonstrated reasonable accuracy in predicting performance under high-thrust conditions, but fail at high advance ratios (J), where the flow around the blade becomes more detached [6]. High-fidelity methods, such as Reynolds-Averaged Navier-Stokes (RANS) simulations, can provide accurate predictions of propeller performance when the wake is properly resolved. Steady (SRANS) and unsteady (URANS) approaches show good agreement with experimental data over a wide range of operating conditions. URANS, in particular, is more accurate when unsteady phenomena are predominant, while SRANS remains suitable when such effects are negligible. However, capturing the wake evolution and reducing numerical dissipation requires refined meshes and significantly increases the computational cost. Even higher-fidelity approaches, such as Lattice-Boltzmann (LB) and Very Large Eddy Simulations (VLES), can better preserve vortex structures, but their accuracy comes at the expense of extremely high computational resources [7].

A valid alternative to grid-based numerical methods are represented by Vortex

Particle Methods (VPMs). The VPMs eliminate the need for generating a computational grid, thereby simplifying the simulation setup, reducing the setup time, and mitigating the numerical dissipation typically introduced by grid-based methods. Even if their ability to predict aerodynamic interaction has been relatively explored [8], their aeroacoustic performance has been only marginally explored.

In this regard, this thesis presents the analysis of a variable fidelity numerical framework based on the VPM, implemented in FLOWUnsteady, and its coupling with an in-house aeroacoustic solver based on the *Ffowcs Williams and Hawkings* analogy (FWH) for tonal noise and the *Amiet approach* for the broadband noise.

This framework aims to provide a valuable variable-fidelity tool to predict aerodynamic and aeroacoustic predictions for advanced propulsion configurations such as DEP systems.

1.2 Objective of the Thesis

Most of the available literature on the propellers' aerodynamic and aeroacoustic interactions [3], [5], [7], [9] focuses on the ability of the grid-based solver to capture the generated complex structures. The VPMs have a relatively large available literature that describes their ability to predict the aerodynamic interaction, but little research describes their predictive capabilities in terms of emitted noise.

The objectives of this thesis are:

- Assess the aerodynamic capabilities of *FLOWUnsteady* by comparing its results with high-fidelity numerical and experimental data.
- Couple the aerodynamic framework with a in-house aeroacoustic solver.
- Investigate the capability of the coupled framework to predict the variations in tonal and broadband noise when an isolated propeller is placed in a distributed configuration.

1.3 Methodology Approach

To validate the capabilities of the framework, the TUD-XPROP-S propeller was used as a case study. It has been used for various experimental campaigns to study the aerodynamic properties of propellers in isolated and distributed configurations [10]. The experimental campaigns carried out on the TUD-XPROP-S make

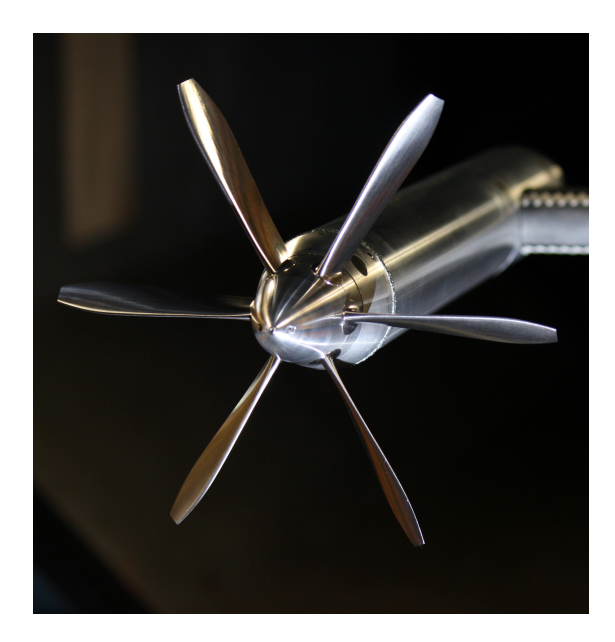


Figure 1.2: TUD-XPROP-S from Delft University of Technology. Image taken from [10].

it the ideal candidate for the validation of the numerical framework.

All of the simulations were conducted at low Mach number and no non-lifting surfaces are modeled. The non-lifting surfaces are not currently modeled in FLOWUnsteady, but it is expected that they will not significantly influence the aerodynamic and aeroacoustic characteristics of the configurations. Therefore, in this work, the interaction effects between acoustic waves and surfaces were not taken into account.

Different advance ratios J were explored in order to characterize the averaged aerodynamic performance in terms of thrust, torque, and propulsive efficiency. Due to the availability of high-fidelity data, the detailed aerodynamic analysis and the aeroacoustic simulations were conducted at an advance ratio J=0.80.

1.4 Outline of the Thesis

The thesis is divided into chapters that follow the chronological order of the work so as to allow the reader to understand the process step by step.

The first chapter introduced the context of the research, focusing on why a numerical tool able to predict the emitted noise with a low computational cost is needed.

The second chapter will introduce the fundamental theoretical background behind the conventional prediction of the aerodynamic performance of a propeller.

The third chapter will introduce the theoretical background needed to understand how FLOWUnsteady works and the execution logic behind the solver.

The fourth chapter will introduce the theoretical background needed to understand the aeroacoustics of a propeller. In the end, the chapter will focus on the numerical model adopted and how the aeroacoustic solver works.

In the fifth chapter, the simulations will be validated against the high-fidelity numerical and experimental data in order to assess the accuracy and reliability of the framework.

The sixth chapter presents the conclusion of the work while giving recommendations for future research.

Chapter 2

Basic Principles of the Propeller Aerodynamics

The aerodynamics of propellers is one of the most investigated topics since the first airplanes. To date, although less used than turbofans in civil aviation, they represent a potential solution to the pollution problem thanks to their high propulsion efficiency.

The complexity of predicting the flow field around a rotor blade stems from the unsteady interactions between the blades, their wakes, and nearby structures such as nacelles and fuselages. In the early stages of aircraft design, propellers are typically analyzed using low-fidelity solvers to identify suitable preliminary configurations. Once the geometry is defined, it is then validated with high-fidelity solvers, such as RANS or LES, to achieve a more accurate understanding of its aerodynamic performance.

In this chapter, the main methods for solving propeller performance are shown in order to get the reader familiar with the basic knowledge of the propeller field.

2.1 Propeller Performance Parameters

The performance of a propeller is not described by the thrust or by the torque exerted, but by non-dimensional parameters that allow comparison between different propellers. The adimensional parameters are derived directly from the *Buckingham* π theorem. Firstly, it is necessary to consider the physical variables that most influence the propeller's performance. They are:

• Propeller's diameter D

- Inflow velocity V_{∞}
- Fluid density ρ
- Fluid dynamic viscosity μ
- Angular speed n
- Speed of sound a

Carrying out the analysis, the following non-dimensional parameters will be found:

Advance Ratio

$$J = \frac{V_{\infty}}{Dn}$$

• Reynolds Number

$$Re = \frac{\rho n D^2}{\mu}$$

• Mach Number

$$M = \frac{nD}{a}$$

These three variables set the performance of a generic propeller.

For describing a propeller's performance, it is usual to use the non-dimensional form of thrust T and torque Q.

$$C_T = \frac{T}{\rho n^4 D^4}$$

$$C_Q = \frac{Q}{\rho n^2 D^5}$$

Another interesting variable is the efficiency:

$$\eta = J \frac{C_T}{C_Q}$$

 C_T represents how much the blade is loaded, C_Q represents how much energy is needed for the rotation of the propeller, and efficiency η describes how much energy is converted into thrust.

The link between the thrust coefficient C_T , the torque coefficient C_Q , and the efficiency η is defined by a functional form as f = f(J, Re, M). These functions are typically presented in diagram form. Some examples are shown in figures 2.1,

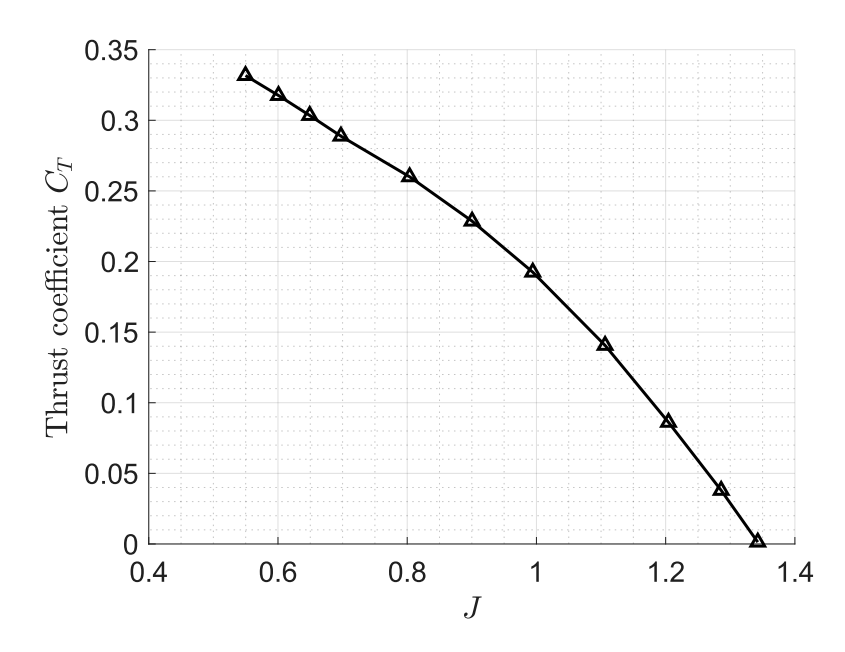


Figure 2.1: Thrust Coefficient C_T versus advance ratio J of the XPROP geometry. Experimental data from Reference [11]

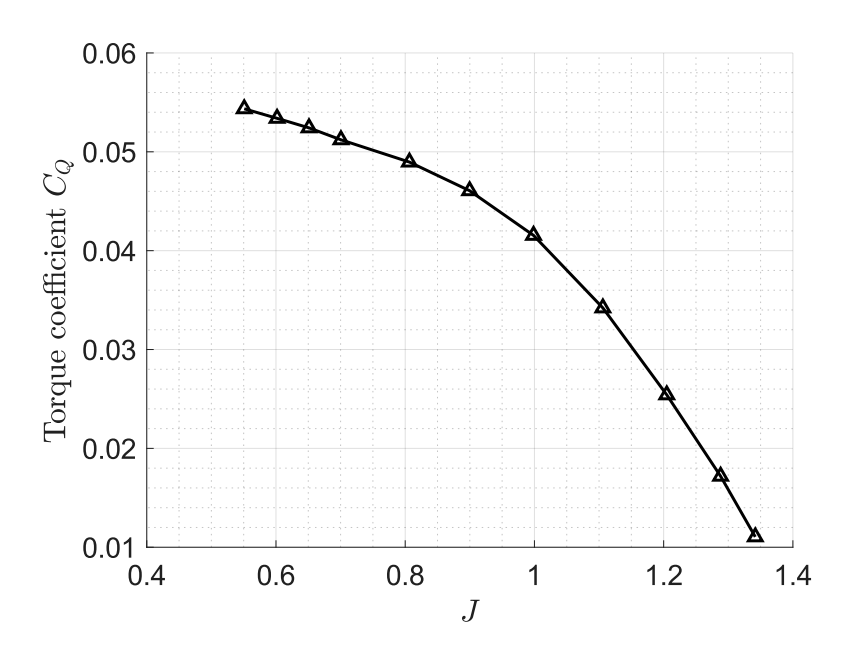


Figure 2.2: Torque Coefficients C_Q versus advance ratio J of the XPROP geometry. Experimental data from Reference [11]

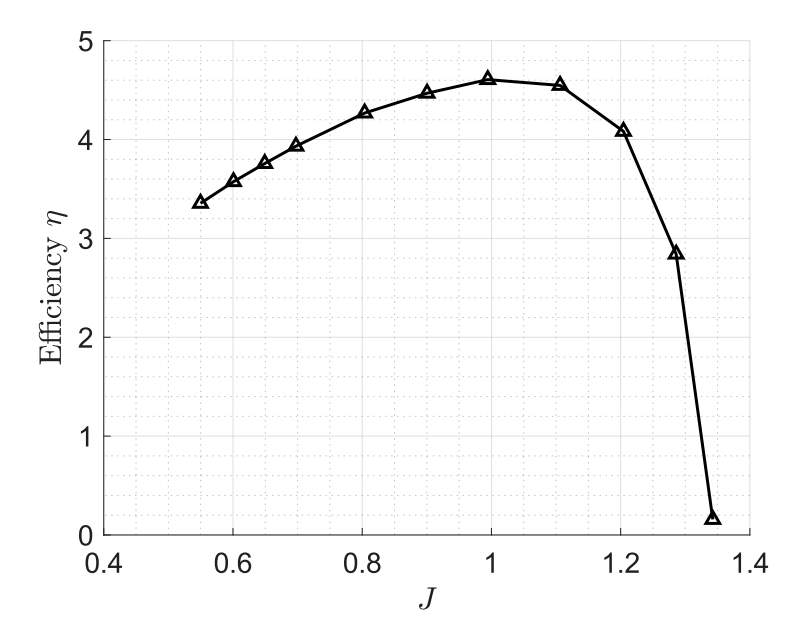


Figure 2.3: Propulsive efficiency η versus advance ratio J of the XPROP geometry. Experimental data from Reference [11]

2.2 and 2.3.

The performance parameter C_T and C_Q can be referred to as the inflow velocity also:

$$T_C = \frac{T}{q_{\infty}\pi R^2}$$

$$Q_C = \frac{Q}{q_{\infty}\pi R^3}$$
(2.1)

Where $q_{\infty} = 0.5 \rho_{\infty} |V_{\infty}|^2$ is the dynamic pressure.

2.2 Mathematical Models For Propellers

In this section, several approaches for evaluating propeller performance are presented, ranging from the simplest methods to the most advanced and accurate ones.

2.2.1 Actuator Disk

In the actuator disk model, the rotor is seen as a one-dimensional, permeable, and infinitesimal disk. In this model, the disk represents a pressure discontinuity in the field.

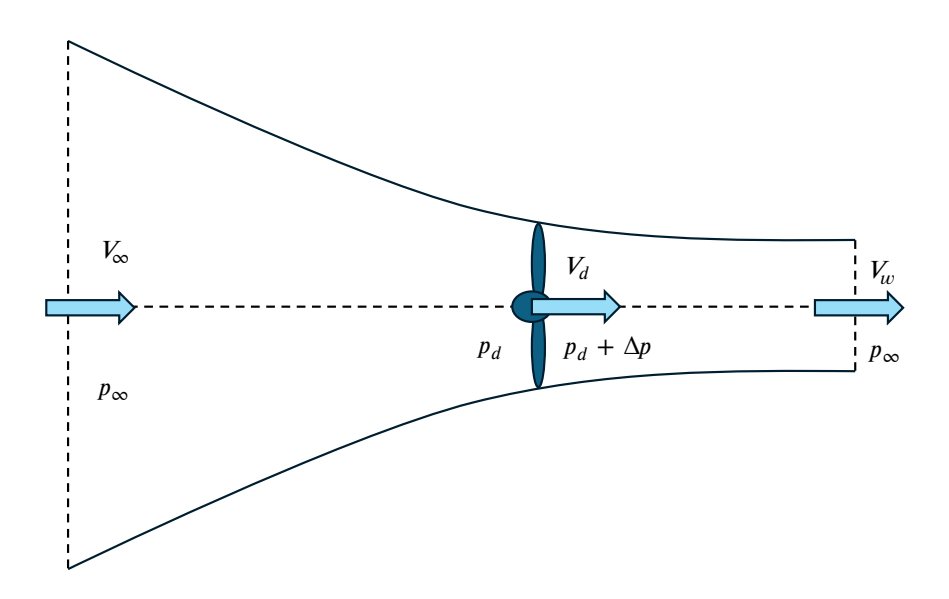


Figure 2.4: Actuator disk scheme.

Using as reference the figure 2.4, suppose that the flow is stationary, incompressible, frictionless, and no external forces act on the stream tube. Applying the momentum equation and the definition of force:

$$T = S\Delta p$$

$$T = \dot{m}(V_w - V_\infty) = \rho SV_d(V_w - V_\infty)$$

Where \dot{m} is the mass flow rate, T is the thrust, ρ is the fluid density, V_w is the velocity at the exit section of the streamtube, and S is the disk surface. Considering the previous hypotheses, it is possible to apply Bernoulli for both the upstream and downstream tube:

$$\Delta p = \frac{1}{2}\rho(V_w^2 - V_\infty^2)$$
10

Equaling the two thrust formulations and substituting the jump pressure disk velocity in the disk section is derived:

$$V_d = \frac{1}{2}(V_w + V_\infty)$$

Defining the velocity increment as:

$$V_d = V_{\infty} + u_d$$

$$V_w = V_\infty + u_w$$

The two velocity increments are related by the following relationship $2u_d = u_w$. Then defining the axial induced velocity factor as $a = u_d/V_{\infty}$, the final thrust formulation is obtained:

$$T = 2\rho SV_{\infty}^2(1+a)a$$

This theory is very simple and takes into account a few parameters. The theory is valid for little velocity increments, then little contraction of the stream tube. Higher contraction of the stream tube can cause instabilities on the shear layer.

The theory does not take into account radial variation or any other induced velocities. The disk actuator model can be extended by considering a tangential induced factor and a radial variation of the parameters as schematized in figure 2.5.

The equations for the thrust and torque are:

$$dT = d\dot{m}V_{\infty}2a$$

$$dQ = d\dot{m}r\Omega r 2a'$$

Where a' is the tangential induced velocity factor and r is the radial coordinate. In this extended version, the fluid flow near the propeller is better resolved, but it does not take into account the possibility that the wake can contract.

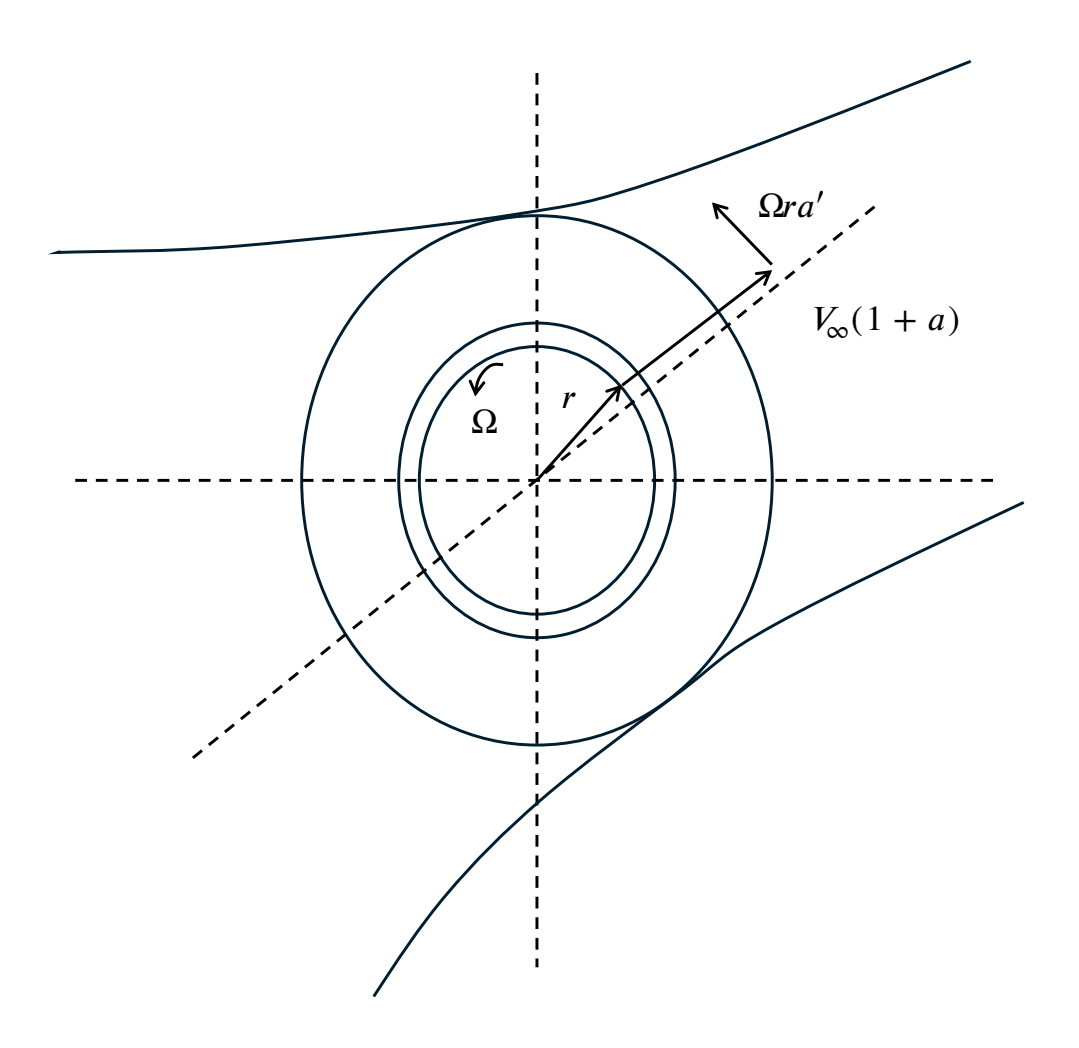


Figure 2.5: Extended actuator disk scheme.

2.2.2 Blade Element Theory

For designing a propeller, engineer must know not only the thrust and torque exerted, but also the specific blade's geometry. The Blade Element Theory (BEM), differently from the actuator disk, takes into account the blade geometry effects on the propeller performance by considering the blades composed of 2D radial elements as shown in figure 2.6.

Neglecting the radial component of the velocity, the blade element can be analyzed

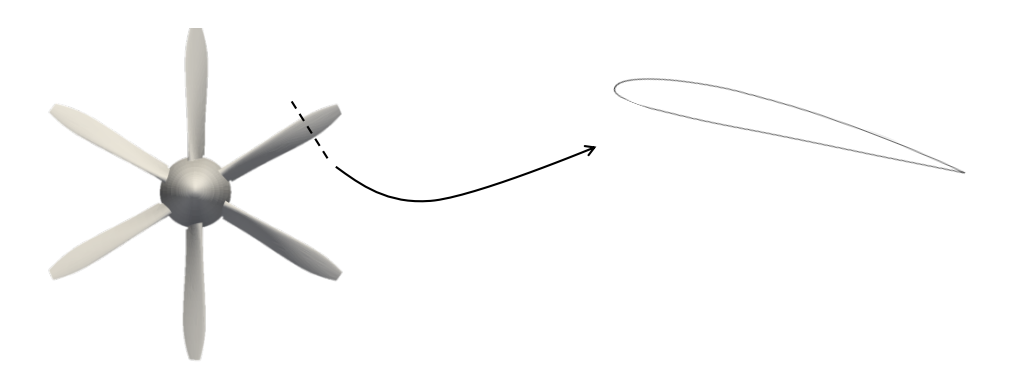


Figure 2.6: Element of the BEM.

as a two-dimensional airfoil. The kinematic properties, and then the Reynolds number also, will vary with the radial coordinate. In this regard, the aerodynamic coefficients must be computed for each blade element.

Using the figure 2.7 as reference, it is possible to derive the thrust and torque formulation:

$$dT = \frac{1}{2}\rho \left[(\Omega r)^2 + V_{\infty}^2 \right] \left(C_l \cos(\phi) - C_d \sin(\phi) \right) c dr$$

$$dQ = \frac{1}{2}\rho \left[(\Omega r)^2 + V_{\infty}^2 \right] \left(C_l \sin(\phi) + C_d \cos(\phi) \right) cr dr$$

Where the lift coefficient $C_l = f(Re(r), \alpha(r))$, the drag coefficient $C_d = f(Re(r), \alpha(r))$, and the chord c = f(r). Defining B as the number of blades and R as the propeller's radius:

$$T = B \int_0^R \mathrm{d}T$$

$$Q = B \int_0^R \mathrm{d}Q$$

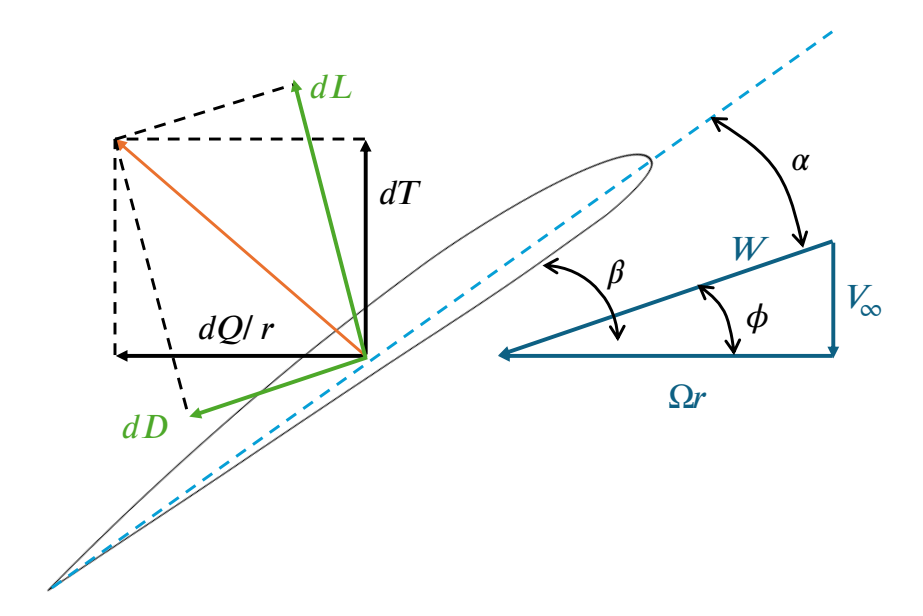


Figure 2.7: Scheme describing the forces and the velocities exerted on a blade element in the Blade Element Theory.

2.2.3 Blade Element Momentum Theory

The Blade Element Momentum Theory (BEMT) combines the actuator disk model and the BEM theory. The actuator disk model is used to compute the axial and tangential velocities, while the BEM theory is used to consider the blade's geometry effects. The method proceeds in an iterative manner. First, an initial guess of the induced velocities must be made; then, using the BEM, the thrust and torque will be computed.

In order to solve the iterative process, the formulations arising from the two theories must be equalized.

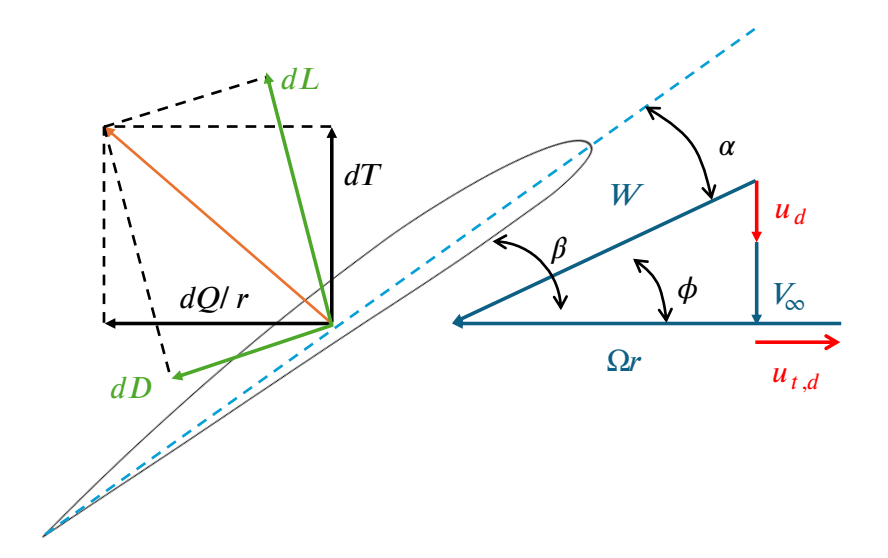


Figure 2.8: Scheme describing the forces and the velocities exerted on a blade element in the Blade Element Momentum Theory.

$$\mathrm{d}T = 4\pi\rho V_{\infty}^2 a(1+a)r\mathrm{d}r$$
 Actuator disk thrust
$$\mathrm{d}Q = 4\pi\rho V_{\infty}\Omega a'(1+a)r^3\mathrm{d}r$$
 Actuator disk torque
$$\mathrm{d}T = \left(C_l\cos(\phi) - C_d\sin(\phi)\right)B\frac{1}{2}\rho W^2c\mathrm{d}r$$
 BEM thrust
$$\mathrm{d}Q = \left(C_l\sin(\phi) + C_d\cos(\phi)\right)B\frac{1}{2}\rho W^2cr\mathrm{d}r$$
 BEM torque

The solution of the problem gives a, a' and ϕ . The values of the induced factors will be used for the next iterations.

$$a = \frac{1}{\left[\frac{4\sin^2(\phi)}{\sigma'\left(C_l\cos(\phi) - C_d\sin(\phi)\right)}\right] - 1}$$

$$a' = \frac{1}{\left[\frac{4\sin(\phi)\cos(\phi)}{\sigma'\left(C_l\sin(\phi) + C_d\cos(\phi)\right)}\right] - 1}$$

$$\tan(\phi) = \frac{V_{\infty}(1+a)}{\Omega r(1-a')}$$

Where $\sigma' = Bc/2\pi r$ is the local solidity of the rotor.

2.2.4 Reynolds-Avaraged Navier-Stokes

The Reynolds-Averaged Navier-Stokes equations (RANS) are a class of methods that solve the Navier-Stokes equation decomposed into a mean component and a fluctuating component. Actually, when the RANS are solved, only the mean component is integrated, while the fluctuating part is modeled with a turbulence model such as Spalart-Almaras, $k-\omega$, and $k-\epsilon$.

Even though the RANS approach is one of the most widely used methods, it requires complex pre-processing and validation of the turbulence model to ensure that the chosen setup is appropriate. The fluid domain must be chosen accurately as a function of the flow regime in order to prevent changes in boundary conditions. The computational grid should be refined in regions where the gradients are higher, such as the boundary layer, and the overall refinement should be high enough to sufficiently reduce the discretization error.

However, RANS represents the most used methodology in industrial design. It can be used for both conceptual design and detailed design due to the high number of models available. The cost is higher compared to low-fidelity methods, but it remains feasible. It should be noted that this approach is valid for high Reynolds number flows.

2.2.5 Large Eddy Simulation

The Large Eddy Simulations (LES) are a class of methods that filters the Navier-Stokes equations. The idea of this approach derives directly from the energy cascade theory. LES directly resolves the turbulence scales up to a given dimension,

imposed by the filter, while the smaller ones are modeled.

The characteristic length of the filter is related to the computational grid dimension, and meeting the required accuracy for resolving the relevant turbulent scales leads to a rapidly increasing computational cost for high-resolving simulations. LES are high-fidelity methods that, however, find limited applications in the industrial world due to their very high computational cost.

Chapter 3

Theoretical Background for FLOWUnsteady

The changing in the aircraft industry leads to a new concept of aircraft such as drones and eVTOL. These aircrafts are characterized by strong aerodynamic interaction between wakes and structural elements. The available low-fidelity tools struggle to resolve all the scales at which aerodynamic interaction occurs; therefore, the need for new frameworks for aircraft design is increasing.

Recent advancements in high-performance computing, such as the introduction of Graphics Processing Units (GPUs) and efficient acceleration algorithms like the Fast Multipole Method (FMM), have renewed interest in Vortex Particle Methods (VPMs). Extensively studied by Winkelmans [12], the VPM represents a Lagrangian approach to solving the vorticity form of the Navier–Stokes equations. In this formulation, the vorticity field is discretized into particles, known as vortons, which are convected and diffused throughout the domain.

Unlike traditional grid-based solvers, the VPM does not require the generation of a computational mesh, thereby avoiding numerical diffusion and preserving the vortex structures in the wake with high fidelity. This property makes the method particularly appealing for simulating complex vortex-dominated flows. Consequently, VPMs have found applications in various fields, including wind farm analysis [13] and, from an aeronautical perspective, the study of propeller-driven aircraft [14].

In this chapter, the basics of the reformulated Vortex Particle Method (rVPM) are introduced following [15]. The main characteristics and current applications will be briefly described in order to give the reader basic knowledge on the FLOWUnsteady

framework. Finally, the procedure for coupling arbitrary methods with the VPM is outlined from a coding point of view.

3.1 FLOWUnsteady

FLOWUnsteady is a variable-fidelity tool that can be used to couple the rVPM with other methods. The necessity to combine the rVPM with other methods relies on its inability to match the boundary conditions imposed by the immersed bodies.

3.1.1 Reformulated Vortex Particle Method

The Vortex Particle Method (VPM) is a meshless approach for solving the vorticity form of the Navier–Stokes equations. The application of this method in aeronautics is limited by its inherent numerical instability when the spatial resolution is increased [15]. Alvarez [16] developed a new set of governing equations to overcome this issue. These equations are directly derived from the Navier–Stokes vorticity equation filtered by a LES filter.

Consider the vorticity form of the Navier–Stokes equations. By denoting the filtering operation with an overbar and applying it to the equation, the following expression is obtained:

$$\frac{\partial \bar{\omega}_i}{\partial t} + \bar{u}_j \frac{\partial \bar{\omega}_i}{\partial x_j} = \bar{\omega}_j \frac{\partial \bar{u}_i}{\partial x_j} + \nu \nabla^2 \bar{\omega}_i - \frac{\partial T'_{ij}}{\partial x_j} + \frac{\partial T_{ij}}{\partial x_j}$$
(3.1)

where T_{ij} is the subfilter-scale vorticity stress, $\partial T_{ij}/\partial x_j$ is the contribution arising from the advective term, and $\partial T'_{ij}/\partial x_j$ represents the contribution arising from vortex stretching. The particle velocity u, computed for the pth particle, is given by:

$$\frac{\mathrm{d}\boldsymbol{x_p}}{\mathrm{d}t} = \boldsymbol{u}(\boldsymbol{x_p})$$

where x_p denotes the position of the pth particle.

To represent the vorticity field as a set of discrete particles, the Dirac delta function $\delta(x)$ is introduced:

$$\omega(\boldsymbol{x},t) \simeq \sum_{p} \Gamma_{p}(t)\delta(\boldsymbol{x} - \boldsymbol{x}_{p}(t))$$
 (3.2)

where Γ_p denotes the vortex strength. Equation 3.2 describes a discrete vorticity field that is nonzero only at the particle positions. The overall vorticity can thus be considered concentrated in discrete point particles. Applying the filter operator ¹, the Dirac delta collapses the integral, yielding the filtered vorticity field:

$$\bar{\omega}(\boldsymbol{x},t) \simeq \sum_{p} \Gamma_{p}(t) \zeta_{\sigma_{p}}(\boldsymbol{x} - \boldsymbol{x}_{p}(t))$$
 (3.3)

where $\zeta_{\sigma_p}(\boldsymbol{x}) = \frac{1}{\sigma^3} \zeta\left(\frac{||\boldsymbol{x}||}{\sigma}\right)$ is the filter kernel of width σ and radial basis ζ . The parameter σ , referred to as the *core size* or *smoothing radius*. The filtering operation spreads the vorticity in space, making it continuous again. This process is equivalent to a LES approach [8]. Substituting Eq. 3.3 into Eq. 3.1, after some algebra, yields the governing equation for the evolution of the vortex strength:

$$\frac{\mathrm{d}\boldsymbol{\Gamma}_{\boldsymbol{p}}}{\mathrm{d}t} = (\boldsymbol{\Gamma}_{\boldsymbol{p}} \cdot \nabla)\boldsymbol{u}(\boldsymbol{x}_{\boldsymbol{p}}) - \frac{3}{5} \left\{ [(\boldsymbol{\Gamma}_{\boldsymbol{p}} \cdot \nabla)\boldsymbol{u}(\boldsymbol{x}_{\boldsymbol{p}})] \cdot \hat{\boldsymbol{\Gamma}_{\boldsymbol{p}}} \right\} \hat{\boldsymbol{\Gamma}_{\boldsymbol{p}}} - \frac{Cd}{\zeta_{\sigma_{\boldsymbol{p}}}} \boldsymbol{E}_{str}(\boldsymbol{x}_{\boldsymbol{p}}). \tag{3.4}$$

Where, E_{str} accounts for the effects of vortex stretching, C_d is a dynamic coefficient in the subfilter-scale vortex stretching model, and $\hat{\Gamma}_p$ is the unit vector of the vortex strength.

Assuming that the core size σ evolves over time, and following [8], the following expression is obtained:

$$\frac{\mathrm{d}\sigma_p}{\mathrm{d}t} = -\left(\frac{1}{5}\right) \frac{\sigma_p}{||\boldsymbol{\Gamma_p}||} \left[(\boldsymbol{\Gamma_p} \cdot \nabla) \boldsymbol{u}(\boldsymbol{x_p}) \right] \cdot \hat{\boldsymbol{\Gamma_p}}$$
(3.5)

Finally, combining Eqs. 3.5, 3.4, and 3.1.1, the governing system of equations for the rVPM is obtained:

¹The filter operator of a field ϕ is defined as $\bar{\phi} = \int_{-\infty}^{\infty} \phi(y) \zeta_{\sigma}(x-y), dy$

$$\frac{\mathrm{d}\boldsymbol{x}_p}{\mathrm{d}t} = \boldsymbol{u}(\boldsymbol{x}_p) \tag{3.6}$$

(3.7)

$$\frac{d\sigma_p}{dt} = -\left(\frac{1}{5}\right) \frac{\sigma_p}{||\Gamma_p||} \left[(\Gamma_p \cdot \nabla) \boldsymbol{u}(\boldsymbol{x_p}) \right] \cdot \hat{\Gamma_p}$$
(3.8)

(3.9)

$$\frac{\mathrm{d}\boldsymbol{\Gamma}_{\boldsymbol{p}}}{\mathrm{d}t} = (\boldsymbol{\Gamma}_{\boldsymbol{p}} \cdot \nabla)\boldsymbol{u}(\boldsymbol{x}_{\boldsymbol{p}}) - \frac{3}{5} \left\{ [(\boldsymbol{\Gamma}_{\boldsymbol{p}} \cdot \nabla)\boldsymbol{u}(\boldsymbol{x}_{\boldsymbol{p}})] \cdot \hat{\boldsymbol{\Gamma}}_{\boldsymbol{p}} \right\} \hat{\boldsymbol{\Gamma}}_{\boldsymbol{p}} - \frac{Cd}{\zeta_{\sigma_{\boldsymbol{p}}}} \boldsymbol{E}_{str}(\boldsymbol{x}_{\boldsymbol{p}}). \tag{3.10}$$

(3.11)

$$\left(\frac{\mathrm{d}\bar{\boldsymbol{\omega}}}{\mathrm{d}t}\right)_{\text{viscous}} = \nu \nabla^2 \bar{\boldsymbol{\omega}} \tag{3.12}$$

Equations 3.6–3.12 define the governing system of the reformulated Vortex Particle Method (rVPM) in Lagrangian form. The viscous term is explicitly considered in Eq. 3.12.

Equation 3.6 governs the evolution of the particle position x_p , which moves with the local velocity $u(x_p)$. Equation 3.8 describes the time evolution of the particle core size σ_p , while Eq. 3.10 governs the evolution of the vortex strength Γ_p . Finally, Eq. 3.12 models the viscous diffusion of vorticity. It should be noted that the first three equations describe the inviscid dynamics of the flow. The main advantage of rVPM over the classical Vortex Particle Method lies in its additional degree of freedom, the particle core size, which allows the conservation laws of mass and momentum to be satisfied more accurately.

There exist different schemes that can solve the viscous part of the flow, such as The Random Walk Method, the Core Spreading Methods and the Particle Strength Exchange. In the rVPM implemented in FLOWUnsteady, the viscous diffusion is solved through the Core Spreading method. Viscous diffusion must be taken into account when the flow is dominated by large low Reynolds number regions or in the case of a bluff body immersed in the flow field. In fact, viscous effects are at the origin of vorticity creation for bluff bodies, and, in the case of intense vortex stretching, the viscous effect provides the only mechanism for dissipating the small-scale energies [17]. The bar on ω denotes the filter operation that makes rVPM a Large Eddy Simulation version of the VPM.

From the vorticity field, it is possible to reconstruct the velocity field as follows:

$$\bar{u} = -\frac{1}{4\pi} \sum_{p} g_{\sigma_p} \left(\boldsymbol{x} - \boldsymbol{x_p} \right) \frac{\boldsymbol{x} - \boldsymbol{x_p}}{||\boldsymbol{x} - \boldsymbol{x_p}||^3} \times \Gamma_p$$
(3.13)

That is the inverted form of the relationship $\omega = \nabla \times \boldsymbol{u}$. g_{σ} is a regularizing function associated with the filter kernel ζ_{σ} . In literature, there are several kernels that could be used, but some of them could present a singularity as $r \to 0$. In order to avoid the singularity, regularized kernels were developed. An example of a regularized kernel is the high-order algebraic kernel by Winckelmans and Leonard.

$$\mathbf{K}_{\sigma} = -\frac{r\left[\left(\frac{r}{\sigma}\right)^{2} + 5/2\right]}{4\pi\sigma^{3}\left[\left(\frac{r}{\sigma}\right) + 1\right]^{*5/2}}\hat{r}$$
(3.14)

As we can see from the functional form of this kernel, as $r \to 0$ there are no singularities.

Bound vorticity

The vorticity field must be fed by the physical phenomena that can create vorticity in the fluid domain. Such phenomena could be the presence of a bluff body, the motion of rotors, or the lift generated by a wing. In order to immerse the vorticity generated by solid boundaries, the filtered vorticity field is decomposed into a free vorticity and a bound vorticity.

$$ar{m{\omega}} = ar{m{\omega}}_{free} + ar{m{\omega}}_{bound}.$$

The bound vorticity not only creates new vorticity, but also influences the evolution of the free vorticity. This vorticity generated by the bound vorticity could be shed in different ways, such as the viscous diffusion in the boundary layer or shed at the trailing edge of the slender bodies. In the last case, no flow separation is taken into account, but the effect of the flow separation could be captured from the airfoil tables [15].

The way in which ω_{bound} is computed defines how the boundary condition is introduced in the LES domain. Currently, the Actuator Line model (ALM) and the Actuator Surface Model (ASM) are implemented in FLOWUnsteady. These two models are described in the following paragraphs.

3.1.2 Actuator Line Model - Rotor Model

FLOWUnsteady takes into account the effect of the rotors with an ALM. The ALM discretizes the blade in blade elements, which are 2D airfoils. Each blade element

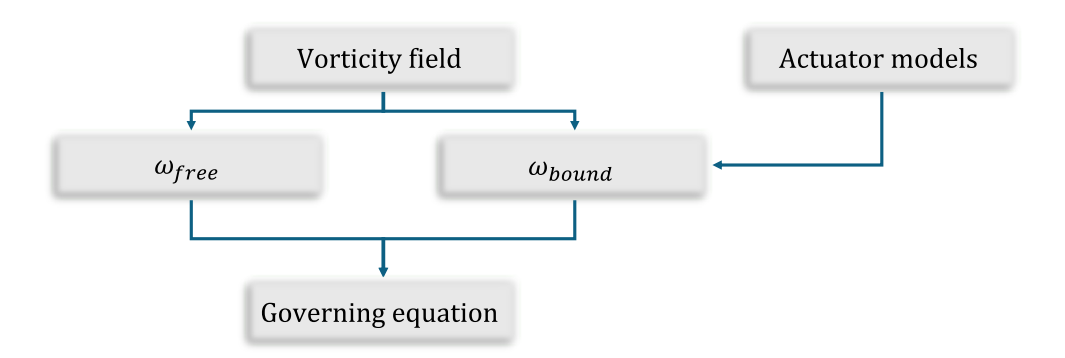


Figure 3.1: Block scheme of immersed vorticity

is characterized by aerodynamic coefficients computed by the panel solver XFOIL developed by Drela [18] or known from experimental data.

The accuracy of the blade element method is entirely dependent on the underlying aerodynamic data; it can account for viscous and compressibility effects only if they are incorporated into that supplied data[15]. Eventually, the lift and drag curves are treated to capture three-dimensional phenomena and post-stall extrapolations [19].

Then, during the simulation, the fluid domain is resolved and the effective Angle of Attack $\theta_{\rm eff}$ (AoA) is computed at the quarter-chord position of each element. The effective angle of attack is used with the tabulated data to determine the sectional lift and drag coefficient. Subsequently, a tip and hub correction was applied in order to take into account the tip and hub effect. In FLOWUnsteady, a modified Prandtl loss function is used [15].

$$F_{\text{tip}} = \frac{2}{\pi} \cos^{-1} \left(\exp(-f_{\text{tip}}) \right), \quad f_{\text{tip}} = \frac{B}{2} \frac{\left[\left(\frac{R_{\text{rotor}}}{r} \right)^{t_1} - 1 \right]^{t_2}}{\left| \sin(\theta_{\text{eff}}) \right|^{t_3}}$$

$$F_{\text{hub}} = \frac{2}{\pi} \cos^{-1} \left(\exp(-f_{\text{hub}}) \right), \quad f_{\text{tip}} = \frac{B}{2} \frac{\left[\left(\frac{r}{R_{\text{hub}}} \right)^{h_1} - 1 \right]^{h_2}}{\left| \sin(\theta_{\text{eff}}) \right|^{h_3}}$$

Where t_1, t_2, t_3, h_1, h_2 , and h_3 are tunable parameters. B is the number of blades, r the radial position of the element, and R_{hub} and R_{tip} are the hub and tip radii. The tunable parameters cannot be determined through a predefined analytical criterion; instead, their values are selected through an iterative process of numerical simulation and empirical expertise. Eventually, the normal and tangential forces are computed as follows:

$$c_n = F_{\text{tip}} F_{\text{hub}} c_l \sin(\theta_{\text{eff}}) - c_d \cos(\theta_{\text{eff}})$$

$$c_t = F_{\text{tip}} F_{\text{hub}} c_l \cos(\theta_{\text{eff}}) + c_d \sin(\theta_{\text{eff}})$$

Where c_l is the lift coefficient, c_d is the drag coefficient, and θ_{eff} is the effective angle of attack. In order to compute these parameters, FLOWUnsteady calls the module CCBlade. CCBlade is a robust Blade Element Momentum (BEM) solver implemented in FLOWUnsteady and developed by Andrew Ning [20].

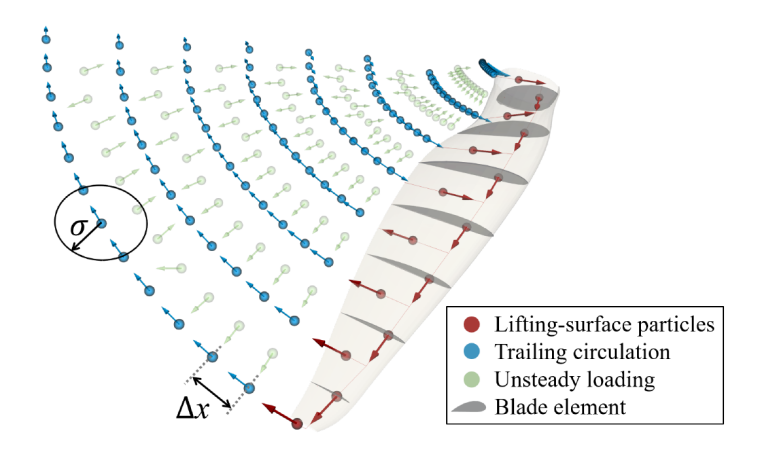


Figure 3.2: Rotor's particles used in ALM. Figure extracted from reference [21]

Once the loadings are known, they are introduced in the vorticity domain by means of the *Kutta-Joukowski theorem*:

$$\Gamma = \frac{cV_{\text{local}}}{2} F_{\text{hub}} F_{\text{tip}},$$

Where V_{local} is the effective velocity seen by the element blade at the quarter-chord position and c is the chord length. Note that the effective velocity is computed

by CCBlade also. The bound vorticity captures the blade circulation computed by the Kutta-Joukowsky theorem, while the shed particle convects the vorticity related to the unsteady loading. Both shedding frequency and core size determine the spatial resolution of the wake.

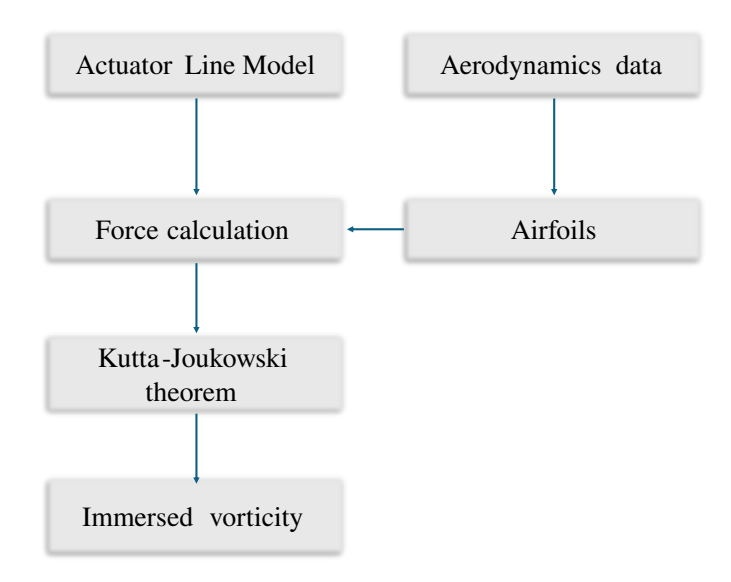


Figure 3.3: Block scheme of the Actuator Line Model.

3.1.3 Actuator Surface Model - Wing Model

Any other complex surface cannot rely on the ALM, as this method does not properly enforce the coupling between the flow and the body. The inherent non-physical nature of the ALM results in an artificial penetration of the flow through the body surface. In many engineering applications, however, the *no-flow-through condition* must be rigorously satisfied, which makes the ALM unsuitable for bodies other than rotors, for which the resulting error is generally negligible.

The Actuator Surface Model (ASM) is introduced in FLOWUnsteady for the bodies that are not well represented by ALM. The no-flow-through condition is obtained by imposing a zero velocity normal to the surface.

The wing is discretized into wing element along the spanwise direction. Each wing element is composed of a bound vortex at the quarter-chord position and two

trailing bound vortices extending to the trailing edges ($\overline{AA'}$, and $\overline{BB'}$).

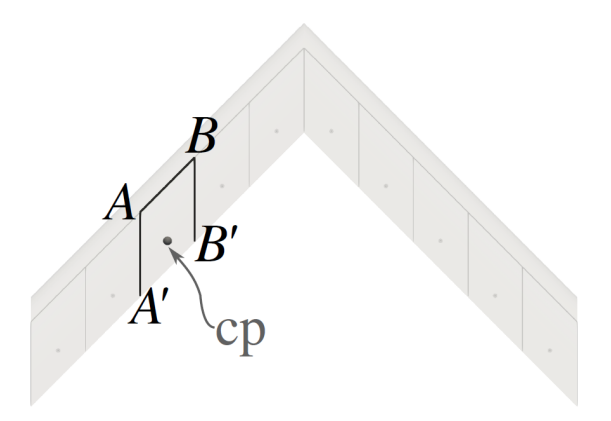


Figure 3.4: Scheme of a wing element of a swept wing in the ASM. Image taken from [8].

In order to immerse the vorticity field induced by the presence of the wing, the circulation on the wing elements must be computed. The velocity induced by the i-th element is computed with the vortex filament approximation as:

$$\boldsymbol{u}_i(\boldsymbol{x}) = \Gamma_i \boldsymbol{G}_i(\boldsymbol{x})$$

where G is defined by the geometric information.

The local velocity is computed at the conventional control point defined at the three-quarter-chord position of each wing element. The local velocity is the sum of self-induced velocity, the kinematic velocity due to the motion of the wing, and the LES velocity computed from the rVPM.

$$oldsymbol{u}_{ ext{local}}^i(t) = oldsymbol{u}_{ ext{wing}}(oldsymbol{x}_{ ext{cp}}^i,t) + oldsymbol{u}_{ ext{kin}}^i(t) + oldsymbol{u}_{ ext{LES}}(oldsymbol{x}_{ ext{cp}}^i,t)$$

Now the no-flow-through condition can be applied, leading to:

$$\boldsymbol{u}_{\text{wing}}(\boldsymbol{x}_{\text{cp}}^{i},t)\cdot\boldsymbol{\hat{n}}_{i} = -(\boldsymbol{u}_{\text{kin}}^{i}(t) + \boldsymbol{u}_{\text{LES}}(\boldsymbol{x}_{\text{cp}}^{i},t))\cdot\boldsymbol{\hat{n}}_{i}$$
 (3.15)

Now, calculating the self-induced velocity as $\boldsymbol{u}_{\text{wing}}(\boldsymbol{x}) = \sum_{i} \Gamma_{i} \boldsymbol{G}_{i}(\boldsymbol{x})$ and replacing it in eq. (3.15):

$$\sum_{i} \Gamma_{i} \boldsymbol{G}_{i}(\boldsymbol{x}) \cdot \boldsymbol{\hat{n}}_{i} = -(\boldsymbol{u}_{\mathrm{kin}}^{i}(t) + \boldsymbol{u}_{\mathrm{LES}}(\boldsymbol{x}_{\mathrm{cp}}^{i}, t)) \cdot \boldsymbol{\hat{n}}_{i}$$

The (3.1.3) is a system of equations of dimension N, where N is the number of wing elements. When the unknown Γ_i are found, the vorticity can be immersed in the

LES domain.

The ASM spreads the vorticity computed from the circulation Γ_i chordwise in order to obtain a more physical flow. Then, the strength of the vortex sheet is calculated as

$$\gamma(x/c) = \Gamma_i g(x/c), \quad \text{with } \int_{-\infty}^{\infty} g(x/c) dx = 1$$

In order to satisfy Kelvin's theorem, at the same time, the trailing circulation is spread onto a vortex sheet as

$$\gamma_t(x/c) = \int_0^{x/c} \gamma(x') \mathrm{d}x',$$

The circulation distribution adopted is *pressure-like* distribution. For more details, read the Reference [8].

The overall force exerted on the wing is composed of three main terms: the aerodynamic force, the viscous force, and the unsteady-circulation force. The aerodynamic force is computed by means of the *Kutta-Joukowski theorem* as follows:

$$\mathbf{F}_{kj} = \rho \mathbf{u}_{\mathbf{x}_b} \times \Gamma \mathbf{\ell}$$

where ℓ is the length of the lifting line segment.

The viscous force can be computed by looking up the aerodynamic table. In the model, it is possible to choose whether to compute the drag coefficient from the local AoA or through the lift coefficient.

The force due to the unsteady change in circulation is computed as follows:

$$\boldsymbol{F}_{\mathrm{uns}} = \rho \frac{\mathrm{d}\Gamma}{\mathrm{d}t} A \hat{\boldsymbol{n}}$$

where A is the area of the wing element.

3.1.4 Framework Execution Logic

FLOWUnsteady is a framework that couples the rVPM with other computational methods such as the *Vortex Lattice Method* (VLM) and the *Blade Element Momentum Method* (BEM). The coupling with those methods is done by means of a particular function called *runtime function*. At each step, the runtime function executes some prescribed commands given by the user. The execution logic

is summarized in the block scheme presented in figure 3.5. In the figure the runtime function() are represented as a circular path in the block scheme.

The first block executed during the calculation is the rVPM solver. In this block, the embedded particles are calculated; they are convected, diffused, and stretched. Subsequently, the first runtime function is called.

At this point, the dynamics of the body must be computed. First of all, the forces and the moment are calculated at the Center of Gravity CG of the body. Subsequently, the linear velocity V and the angular velocity Ω of the body are calculated. If any prescribed kinematic by the user was given, it will be used instead of the calculation previously mentioned.

When the dynamics are known, the circulation must be solved. To do this, another runtime_function() is called. In this function, solvers such as CCBLADE for BEM or Vortex Lattice Method for VLM are called for computing the circulation.

When all these steps are done, the solver checks if the maximum time is reached. If it is not, then all the calculations are repeated. If it is, the computation stops.

The block system that composes the framework makes it very easy to modify. In fact, if you want to change the models in the aerodynamic solution, you only have to change the runtime_function() that gives the circulation value. The kinematic step and the VPM solver are not related to the code that resolves the circulation over the body. In Figure 3.5, the runtime_function() is represented as a circular path in the code.

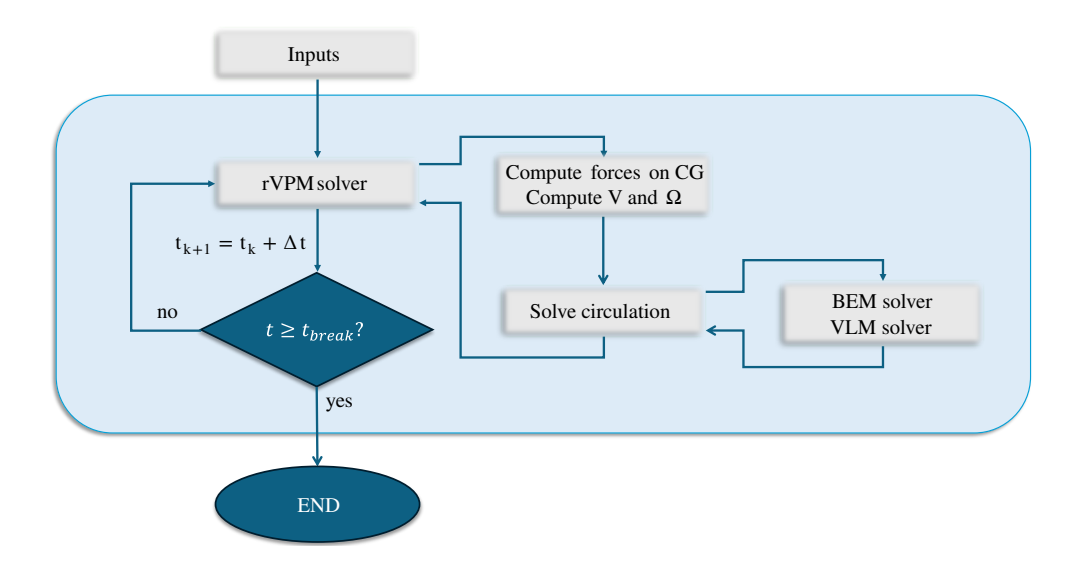


Figure 3.5: Block scheme showing the execution logic of FLOWUnsteady. The figure shows the main steps linked in chronological order by arrows. The runtime_function() are represented by the circular path. Exemplified version of the block scheme of the official documentation.

Chapter 4

Physics and Modeling of the Propeller Noise

Recent developments in the aeronautical world have led to increasingly stringent certification regulations. In particular, due to the evolution of propulsion systems, the increase in air traffic, and the introduction of new generation aircraft concepts, the noise emitted could become one of the main disturbances for the civilian population [1].

The propulsion system represents one of the main sources of noise generated by an aircraft. The prediction of such noise is possible by means of the *Ffowcs-Williams* and *Hawkings theory*, based on the *Lighthill's analogy* and some empirical correlations.

In this chapter, the fundamentals of the *Ffowcs Williams and Hawkings theory* are presented, followed by an explanation of how it can be applied to predict both tonal and broadband noise generated by a propeller.

4.1 Physics of Sound

What people know and perceive as *sound* are nothing more than mechanical waves propagating in a medium. Physically, the mechanical waves are generated by a small perturbation in the field, such as a displacement of solid surfaces or a displacement of the medium itself. When the perturbation is generated, a little compression and rarefaction happen in the near region. Due to the elasticity of the medium, the particles compressed by the perturbation tend to return to the rest position due to the lower pressure, but with an overshoot. The particles' movements can be seen as the well-known spring motion. A schematic view of the

particles' field is shown in figure 4.1.

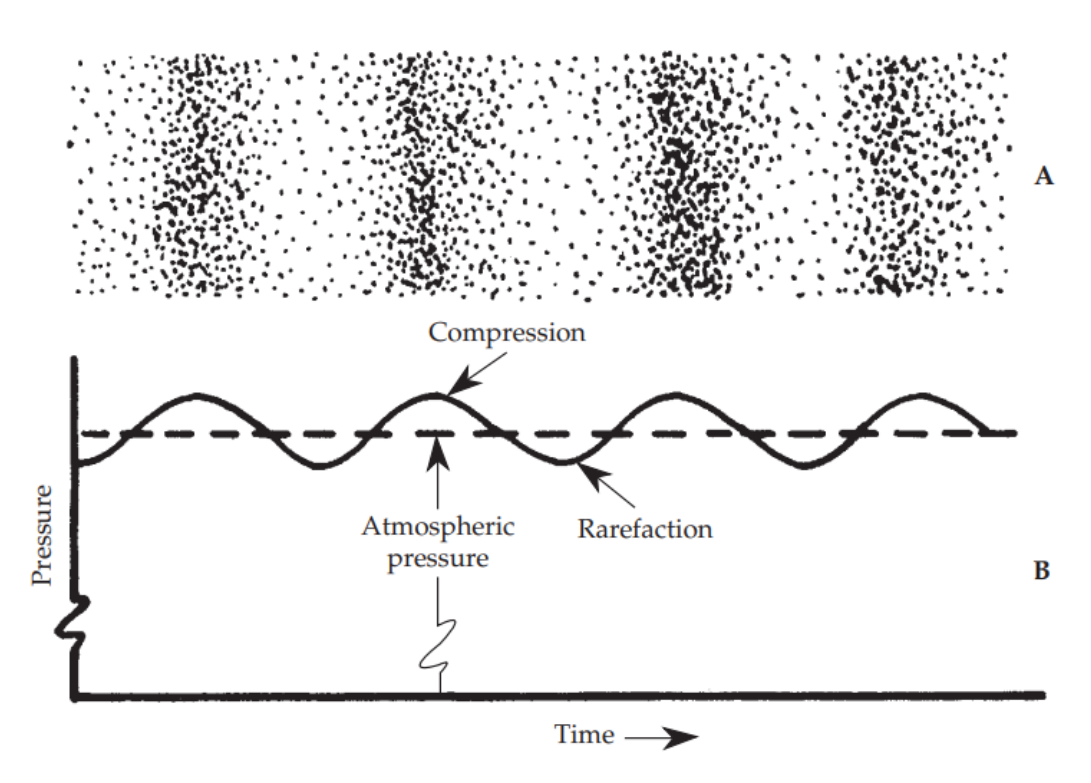


Figure 4.1: Instantaneous view of the particles and the pressure variations. Figure extracted by Reference [22]

Then, sound exists because of the elastic properties of the medium which allow particles to fluctuate around a rest position and transfer momentum from one particle to another.

The idea of the sound as a propagating mechanical wave has been useful in many engineering fields, including aeroacoustics. One of the most important applications of this idea is the *Lighthill's acoustic analogy*.

The Lighthill's analogy reformulates the Navier-Stokes equations as an inhomogeneous wave equation.

$$\frac{\partial^2 \rho'}{\partial t^2} - c_{\infty}^2 \frac{\partial^2 \rho'}{\partial x_i^2} = \frac{\partial^2 T_{ij}}{\partial x_i \partial x_j}$$

$$\tag{4.1}$$

Where T_{ij} is Lighthill's tensor, $\rho' = \rho - \rho_{\infty}$ is the density fluctuation.

The right side of the equation is treated as a source term. On the left side, there is a wave operator for the density fluctuation as the dependent variable. It is important to note that Lighthill's analogy has no approximation, but it is an exact reformulation of the Navier-Stokes equations.

Ffowcs Williams and Hawkings generalized Lighthill's analogy to include not only the free stream generated noise, but also the noise generated by moving boundaries. This generalization represents a fundamental equation in the field of aeroacoustics, as it enables the calculation of noise generated by moving objects, such as propellers.

4.1.1 Ffowcs-Williams and Hawkings

The Ffowcs-Williams and Hawkings (FWH) analogy is a generalization of the earlier Lighthill analogy. Lighthill's analogy is based on the exact equations of fluid flow, without making any assumptions about the flow regime. Ffowcs-Williams and Hawkings extended Lighthill's result to account for moving surfaces within the domain by using generalized derivatives and incorporating the effects of surface motion [23].

Using the method of Green's functions, the final result from this theory, applied to an impenetrable and moving surface, is the following:

$$\rho'(\boldsymbol{x},t)c_{\infty}^{2} \approx \frac{x_{i}x_{j}}{|\boldsymbol{x}|^{2}} \frac{1}{c_{\infty}^{2}} \frac{\partial^{2}}{\partial t^{2}} \int_{V_{0}} \left[\frac{T_{ij}}{4\pi |\boldsymbol{x}|(1-M_{r})} \right]_{\tau=\tau^{\star}} dV(\boldsymbol{z})$$

$$+ \frac{x_{i}}{|\boldsymbol{x}|} \frac{1}{c_{\infty}} \frac{\partial}{\partial t} \int_{S_{0}} \left[\frac{p_{ij}n_{j}}{4\pi |\boldsymbol{x}|(1-M_{r})} \right]_{\tau=\tau^{\star}} dS(\boldsymbol{z})$$

$$+ \frac{\partial}{\partial t} \int_{S_{o}} \left(\frac{\rho_{\infty}V_{j}n_{j}}{4\pi |\boldsymbol{x}|(1-M_{r})} \right)_{\tau=\tau^{\star}} dS(\boldsymbol{z})$$

$$(4.2)$$

where τ^* is the emission time, M_r is the source Mach number of the source in the direction of the observer, c_{∞} is the speed of sound in the propagation field, p_{ij} is the stress tensor, T_{ij} is Lighthill's stress tensor, S is the impenetrable moving surface with unit vector n_j , V_j is the velocity and x_j and x_i are spatial coordinate.

The first integral is defined as a quadrupole term source; it is the sound radiated by the turbulence and flow distortion. At low Mach, this term has the lowest magnitude with respect to the other sources. The second integral is a dipole source term; it is the sound radiated by the loading on the surface. It has a magnitude of an order greater with respect to the quadrupole term.

The third term is defined as a monopole source; it is the sound radiated by the fluid displacement due to the body motion [23]. For low Mach number flows, it has the highest magnitude with respect to the dipole and quadrupole sources.

Each term takes into account the Doppler effect by means of the term $1 - M_r$. Increasing the relative Mach number increases the signal frequency due to a higher magnitude of the time derivative.

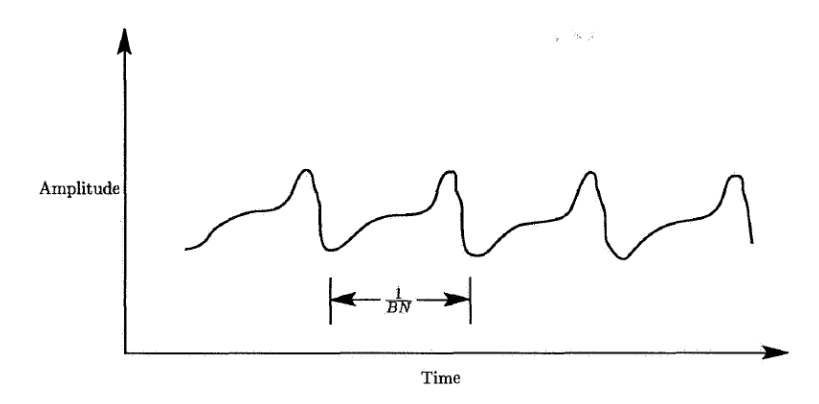
4.1.2 Mechanisms of Noise Generation in Rotors

The motion of a rotating and moving rotor in a fluid flow generates two types of acoustic signals. The first one is known as *tonal noise* and the second one is *broadband noise*.

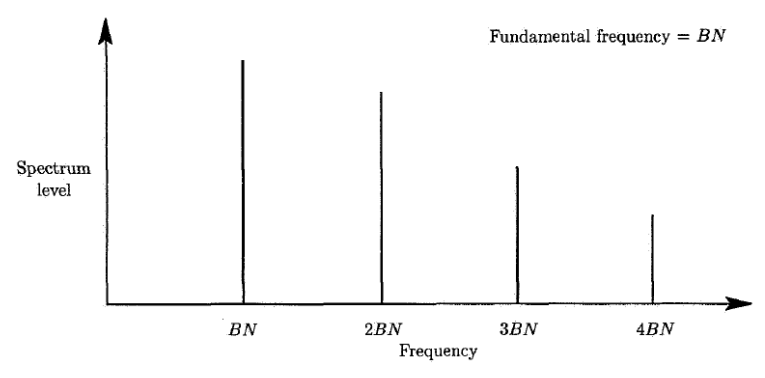
The tonal noise is mainly caused by the periodic nature of the rotating motion of the rotors. It is recognizable by the characteristic signature defined by a high intensity focused on the Blade Passing Frequency (BPF) and its multiples. The BPF is defined as the product of the number of blades N_{blades} and rotation speed n: $BPF = N_{blades} \cdot n$. Physically, the BPF defines how many times an observer sees a blade during a single revolution. The tones at the multiples of the BPF are generated by the unsteady interaction between the blades. In figure 4.2a is shown an example of a harmonic signal.

The broadband noise, differently from tonal noise, is characterized by an energy content spread over a large range of frequencies. It is mainly generated by blades' interaction with turbulence. There are many interaction phenomena that can generate broadband noise such as trailing edge noise, vortex ingestion noise, and haystacking. Due to its stochastic nature, it is very difficult to predict it. An example of a broadband signal is shown in figure 4.3. Sometimes it is called self-generated noise because it is generated by the strong change in boundary condition due to the interaction between the blade and the blade's turbulence boundary layer.

For low Mach number flows, the effects of turbulence or fluid volume displacements are small, so the main source of noise is represented by the loading noise. The loading noise is generated by the time variation both in magnitude and in



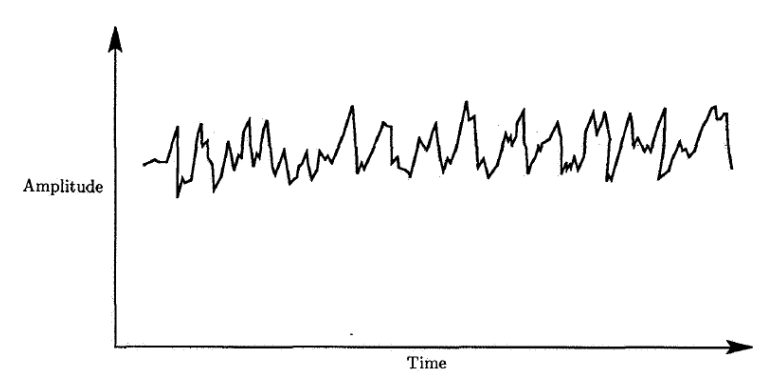
(a) Generic signal from a tonal noise source.



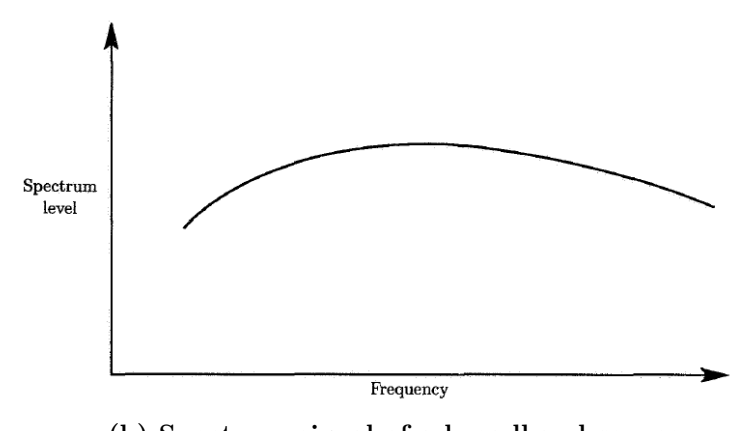
(b) Spectrum signal of a tonal noise.

Figure 4.2: Example of a tonal source signal. Extracted from Reference [24].

direction of the loading on the blades. Typically, the steady component of the loading generates noise due to the change in direction of the drag and thrust components.



(a) Generic signal from a broadband noise source.



(b) Spectrum signal of a broadband source.

Figure 4.3: Example of a broadband source signal. Extracted from Reference [24].

4.2 Aeroacoustic Framework

The in-house framework developed combines two sub-routines. The first sub-routine computes the two components of the tonal noise with a time-domain approach, while the second one computes the broadband noise in terms of trailing edge noise with a frequency domain method.

The tonal noise solver was developed in [25]. Its code utilized the FWH theory following the procedure described in [23]. Two hypotheses were considered: the observer is placed in the far field, and the surface integrals are calculated on the blade surface planform.

The broadband noise solver was developed by Belleli F. The code utilized is a follow-up to the one presented in Reference [26]. Its routine uses an Amiet Approach fed with a Wall Pressure Fluctuation function. The routine comprehends a leading edge back-scattering as well.

4.2.1 Tonal Noise

The tonal solver computes the loading noise and the thickness noise.

$$(p'(\boldsymbol{x},t))_{loading} = \frac{x_i}{|\boldsymbol{x}|} \frac{1}{c_{\infty}} \frac{\partial}{\partial t} \int_{S_0} \left[\frac{p_{ij}n_j}{4\pi |\boldsymbol{x}|(1-M_r)} \right]_{\tau=\tau^*} dS(\boldsymbol{z})$$
(4.3)

$$(p'(\boldsymbol{x},t))_{thickness} = \frac{\partial}{\partial t} \int_{S_o} \left[\frac{\rho_{\infty} V_j n_j}{4\pi |\boldsymbol{x}| |1 - M_r|} \right]_{\boldsymbol{x} = \boldsymbol{\tau}^{\star}} dS(\boldsymbol{z})$$
(4.4)

Retarded Time

Each component of the tonal noise requires the accurate computation of the blade's element position. The coordinate system is represented in figure 4.4. In order to compute the exact position of the rotors, firstly the rotor geometry parameters must be provided. For each rotor, the module that creates the geometry requires: the hub and tip radii, the position of the center of gravity of the rotor, number of rotors, number of blades, and the phase shift for each blade. Subsequently, by means of the kinematic module, the rotors are translated and rotated in space according to the maneuver. The kinematic module requires for each rotor the linear velocity of the center, the rotation speed on x_2 and x_3 axes, and the rotation speed of the rotor. One should note that it is possible to define different maneuver stages, each of them characterized by different velocities. In this work, only one maneuver stage is needed.

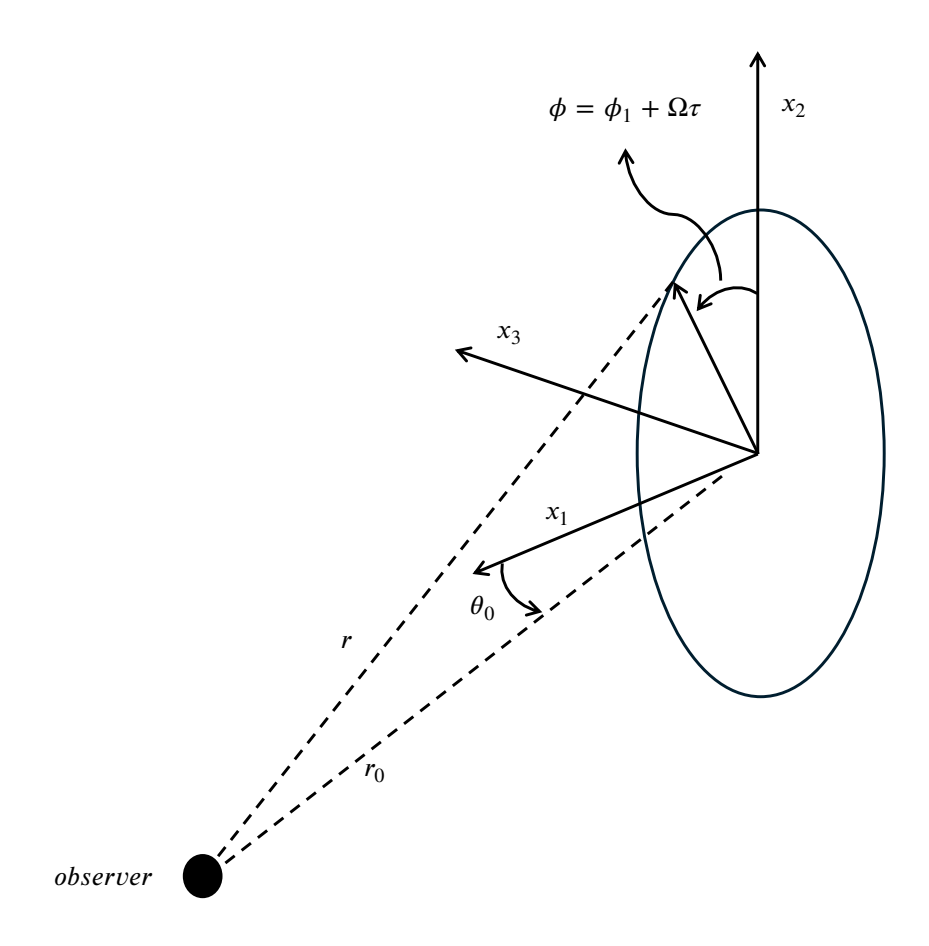


Figure 4.4: Coordinate system [23].

When the position of the blade elements is computed by the previous module, the retarded time equation can be solved:

$$t - \tau - \frac{|\boldsymbol{x} - \boldsymbol{y}(\tau)|}{c_{\infty}} = 0 \tag{4.5}$$

Where \boldsymbol{x} is the observer position, \boldsymbol{y} is the element location, t is the observer time, and τ is the emission time. Due to the non-linearity of the equation, it is solved by an iterative method.

Once the retarded time is known, it is possible to compute the tonal noise contribution by means of the solver module.

Loading Noise

To compute the loading noise, the blade's surface is approximated by its projection in the rotor's plane as schematized in figure 4.5.

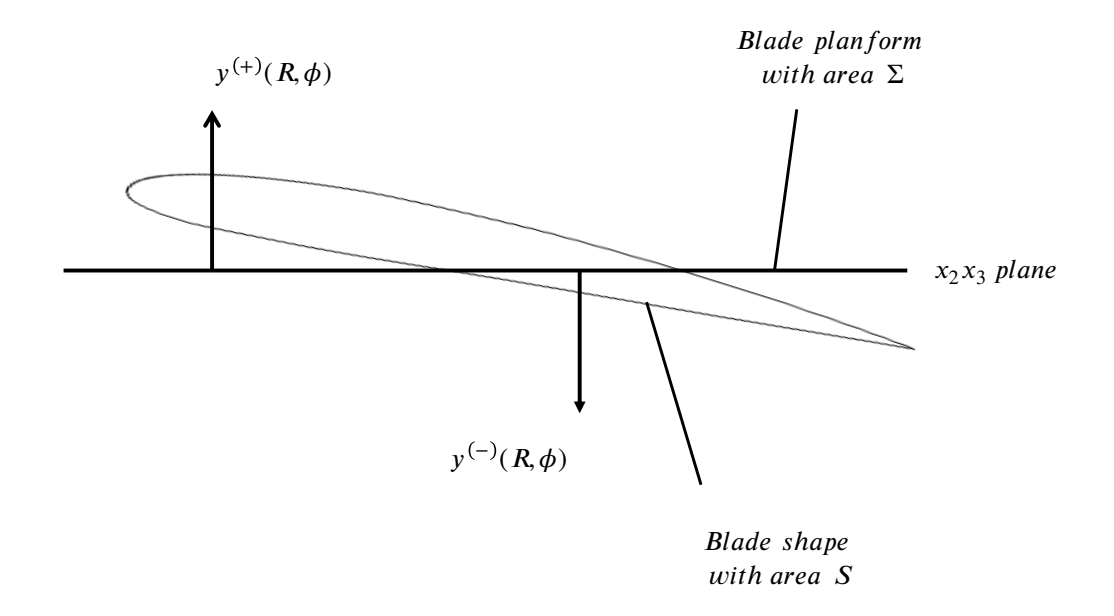


Figure 4.5: Scheme of blade planform [23].

Defining the surface loading as $f_i = ([p_{ij}n_j]_{upper} - [p_{ij}n_j]_{lower})$ and substituting into the loading pressure terms 4.3:

$$(p'(\boldsymbol{x},t))_{loading} = \frac{x_i}{|\boldsymbol{x}|} \frac{1}{c_{\infty}} \frac{\partial}{\partial t} \int_{\Sigma_0} \left[\frac{f_i(\boldsymbol{z},\tau)}{4\pi |\boldsymbol{x}| (1-M_r)} \right]_{\tau=\tau^{\star}} d\Sigma(\boldsymbol{z})$$

Following the procedure in Reference [23], the approach of Farassat is used in order to address the difficulty in calculating the surface loading as a function of the retarded time. The Farassat approach consists of shifting the spatial derivatives to source time. The result is:

$$(p'(\boldsymbol{x},t))_{loading} \approx \frac{1}{c_{\infty}} \int_{\Sigma_0} \left[\frac{x_i}{4\pi |\boldsymbol{x_i}|^2 (1-M_r)^2} \left\{ \frac{\partial f_i}{\partial \tau} + \frac{f_i}{(1-M_r)} \frac{\partial M_r}{\partial \tau} \right\} \right]_{\tau=\tau^*} d\Sigma(\boldsymbol{z})$$

Where Σ_0 is the whole blade planform. The blade loading and the relative Mach number derive directly from the aerodynamic solution. Following the same approach, the derived formulation is:

Thickness noise

The thickness noise is computed exactly as the loading noise, but with a different source term.

$$(p'(\boldsymbol{x},t))_{thickness} = \frac{\partial}{\partial t} \int_{\Sigma_0} \left[\frac{\rho_{\infty} \boldsymbol{V} \cdot \nabla h}{4\pi r |1 - M_r|} \right]_{\tau = \tau^*} d\Sigma(\boldsymbol{z})$$

One should note that the thickness noise does not depend on the blade thickness h, the fluid density ρ_{∞} , and its velocity V. Other airfoil's geometric parameters, such as camber and angle of attack, are not taken into account in this formulation. As done for the loading noise, the formulation based on Farassat's approach will be used for simplifying the evaluation of the integrand at the correct retarded time.

$$(p'(\mathbf{x},t))_{\text{thickness}} = \sum_{k} \rho_{\infty} \Delta V_{k} \left[\frac{1}{(1-M_{r})} \frac{\partial}{\partial \tau} \left(\frac{1}{(1-M_{r})} \frac{\partial}{\partial \tau} \left(\frac{1}{4\pi r |1-M_{r}|} \right) \right) \right]_{\mathbf{y}=\mathbf{y}^{(k)}}^{\tau=\tau^{*}}$$

Finally, introducing the far field approximation, the final formulation for thickness noise is derived:

$$(p'(\mathbf{x},t))_{\text{thickness}} = \sum_{k} \rho_{\infty} \Delta V_{k} \left[\frac{1}{4\pi r} \left(\frac{1}{(1-M_{r})^{4}} \frac{\partial^{2} M_{r}}{\partial \tau^{2}} + \frac{3}{(1-M_{r})^{5}} \left(\frac{\partial M_{r}}{\partial \tau} \right)^{2} \right) \right]_{\mathbf{v} = \mathbf{v}^{(k)}}^{\tau = \tau^{*}}$$

4.2.2 Broadband Noise

The broadband solver is based on the information given in Reference [27].

The Broadband solver resolves a boundary value problem in an idealized case by means of the Amiet Approach. Firstly, suppose that the airfoil is a semi-infinite flat plate.

The model starts with the classic assumptions of Lighthill, who supposed that the total pressure satisfies the following equation:

$$\frac{1}{c}\frac{\mathrm{D}^2 p}{\mathrm{D}t^2} - \nabla^2 p = \frac{\partial T_{ij}}{\partial x_i x_j} \tag{4.6}$$

Where the Lighthill's tensor is approximated by $T_{ij} \approx \rho u_i u_j$. The coordinate system is defined by x_1 positive in the direction of the flow, x_2 in the direction

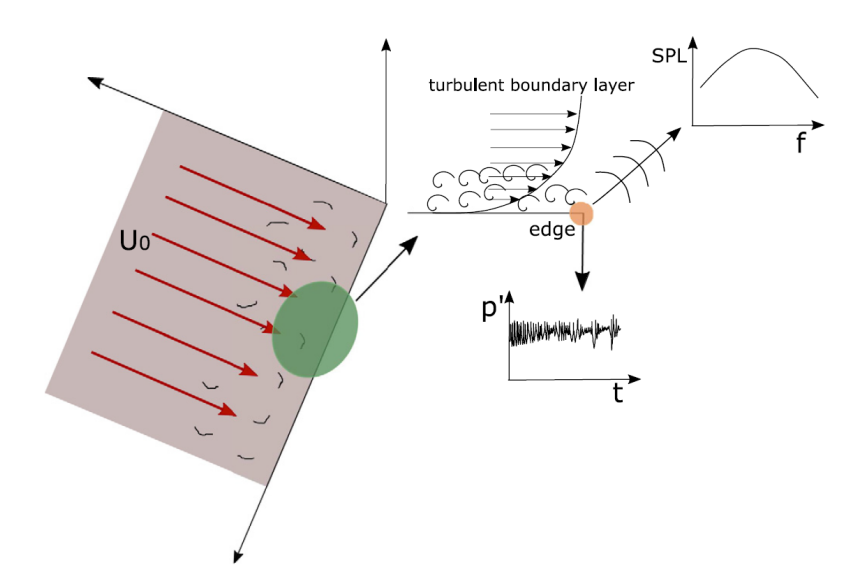


Figure 4.6: Schematic of trialing-edge noise generation. Figure extracted by Reference [27].

normal to the plane, and x_3 the spanwise direction. If the surrounding fluid has a steady uniform flow, then the boundary conditions are:

$$\left. \frac{\partial p}{\partial x_2} \right|_{x_2} = 0, \quad x_1 < 0$$

$$\Delta p \Big|_{x_2=0} = 0, \quad x_1 > 0$$

The first boundary condition enforces the no through-flow, while the second one supposes the existence of a flat vortex sheet extending in x_1 direction with a constant $x_2 = 0$.

Using the Amiet approach, the final formulation for the Power Spectral Density S_{pp} is:

$$S_{pp}(\omega, \boldsymbol{x}) = \left(\frac{\omega x_3 b}{2\pi c_0 \sigma_0^2}\right) 2L |\mathcal{L}|^2 \Phi_{pp}(\omega) l_2(\omega).$$

Where \mathcal{L} is the radiation integral, Φ_{pp} is the Wall Pressure Fluctuation model (WPF), l_2 is the spanwise correlation length, L is the span-wise semi-chord ratio,

and b is the semi-chord. The equation takes into account both the pressure side and suction side contributions.

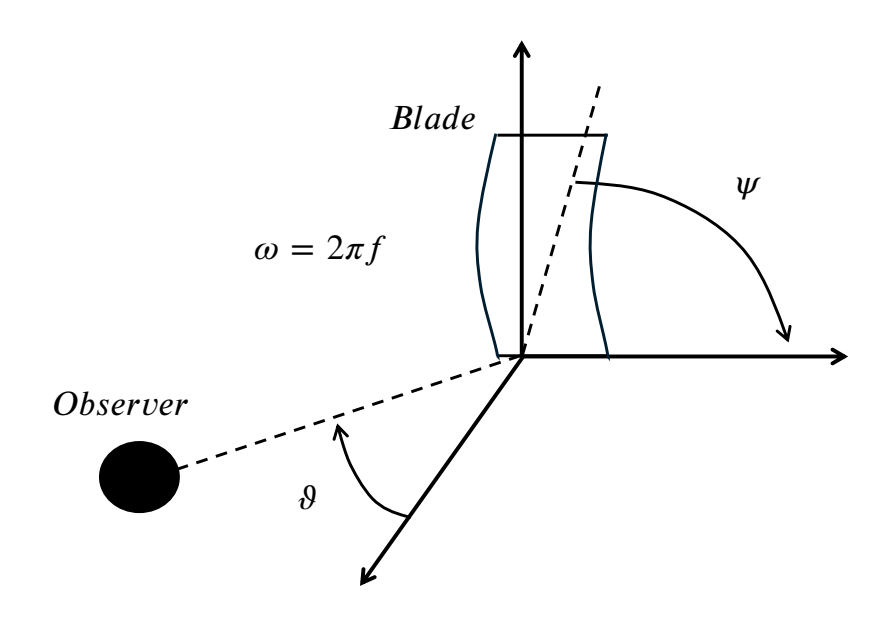


Figure 4.7: Coordinate system of the Amiet Approach for propellers.

In order to compute the power spectral density, some steps must be accomplished. The first one is to calculate the wall pressure function Φ_{pp} , the second one is to compute the radiation integral \mathcal{L} , and the last one is to compute the spanwise correlation length l_2 .

The wall pressure function used in the solver requires the boundary layer's parameters. In this work, they are computed by XFOIL, the panel solver developed by Drela [18]. Some parameters are not directly computed by XFOIL, such as the gradient pressure $\mathrm{d}p/\mathrm{d}x$ and the boundary layer thickness δ , so that they are calculated as:

$$\delta = \theta \left(3.15 + \frac{1.72}{H - 1} + \delta^* \right)$$

$$\frac{\mathrm{d}p}{\mathrm{d}x} = \frac{1}{2}\rho U_0^2 \frac{\mathrm{d}c_p}{\mathrm{d}x}$$

Where θ is the momentum thickness, δ^* is the displacement thickness, and $H = \delta^*/\theta$. The derivative involved in the computation of the pressure gradient can be approximated by a finite difference; in this work, a central difference was used. Finally, once the boundary layer's parameters are known, the wall pressure spectra can be calculated as:

$$\Phi_{pp}(\omega) = \frac{a(\omega FS)^b}{[i(\omega FS)^c + d]^e + [(fR_T^g)(\omega FS)]^h}$$
(4.7)

The coefficients, function of the boundary layer's parameters, are shown in the appendix A. In the broadband module, were implemented: Goody, Rozenberg, Kamruzzaman, Catlett, Hu, and Lee models.

The spanwise correlation length can be computed in its default form or regularized form as:

$$l_2(\omega) = \frac{U_c}{b\omega}, \quad \text{no-regularized}$$

$$l_2(\omega) = \frac{U_c}{b\omega} \left\{ 1 - \exp\left[\frac{\left(\frac{\omega \delta^*}{Ue}\right)^2}{0.09}\right] \right\}, \quad \text{regularized}$$
(4.8)

The constant 0.09 represents an additional degree of freedom in the models, and its appropriate value must be calibrated for the specific case under investigation.

$$U_c = \alpha' U \tag{4.9}$$

Where b and α' are arbitrary parameters.

The radiation integral is computed following the procedure described in Reference [28]. The mathematical model uses three-dimensional gusts for simulating the incident aerodynamic wall pressure scattered. The solution for the radiation integral is:

$$I(\bar{K}_1, \bar{K}_2) = \int_{-2}^{0} f(X)e^{-iCX}dX,$$
 with $f = f_1 + f_2$.

Where f_1 is the main term, f_2 is the leading-edge backscattering correction, and K_1 and K_2 denote the streamwise and spanwise aerodynamic wavenumbers, respectively. The values of the constants are reported in Appendix B.1. The functions f_1

and f_2 depend on the type of gust considered, which is defined by comparing the spanwise wavenumbers with a frequency parameter. For a supercritical gust, i.e. $|\bar{K}_2| < \bar{K}M/\beta$, the main term and the leading-edge backscattering correction are given by:

$$\begin{split} &\int_{-2}^{0} f_1(X) e^{-iCX} dX \\ &= -\frac{e^{2iC}}{iC} \left\{ (1+i) e^{-2iC} \sqrt{\frac{B}{B-C}} E^{\star} [2(B-C)] - (1+i) E^{\star} [2B] + 1 \right\} \\ &\frac{1}{H} \int_{-2}^{0} f_2(X) e^{-iCX} dX \\ &= e^{4i\bar{k}} [1 - (1+i) E^{\star} (4\bar{k})]^C - e^{2iD} + i [D + \bar{K} + M\bar{\mu} - \bar{k}] G \end{split}$$

While for a subcritical gust, i.e. $|\bar{K}_2| < \bar{K}M/\beta$, are:

$$\int_{-2}^{0} f_1'(X)e^{-iCX}dX$$

$$= -\frac{e^{-2iB}}{iC} \left\{ e^{-2iC} \sqrt{\frac{A_1'}{\bar{\mu}(x_1/S_0) - i\bar{k}'}} \Phi^0([2i(\bar{\mu}(x_1/S_0) - i\bar{k})]^{1/2}) - \Phi^0([2iA_1']^{1/2}) + 1 \right\}$$

$$\begin{split} &\int_{-2}^{0} f_2'(X) e^{-iCX} dX \\ &= \frac{e^{-2iB]}}{B} H' \left\{ A'(e^{2iB} [1 - erf\left(\sqrt{4\bar{k}}\right)] - 1) + \sqrt{2\bar{k}} \left(\bar{K} + \left(M - \frac{x_1}{S_0}\right)\bar{\mu}\right) \frac{\Phi^0(\sqrt{-2iB}}{\sqrt{iB}} \right\} \end{split}$$

Where E^* is the complementary complex error function [28]. The procedure is not straightforward, and for this reason, the mathematical steps are not reported in this work. However, it is important to know that the model has some restrictions; in fact, the blade tip effects are ignored, and the blade is considered as an isolated airfoil.

Once the power spectral density was calculated, supposing that all the blades are equal and that they have the same time history during the revolution, the power spectral density of the rotor is:

$$S(\omega) = \sum_{i=1}^{Ns} \frac{B}{2\pi} \int_0^{2\pi} \left(\frac{\omega_e(\psi)}{\omega} \right)^2 S_{pp}(\omega_e(\psi), \boldsymbol{x}(\psi)) d\psi$$

Where B is the number of blades, $\omega_e = \omega(1 + M \sin(\theta) \sin(\psi))$, and ψ is the angular coordinate.

Chapter 5

Validation of the Coupled Framework

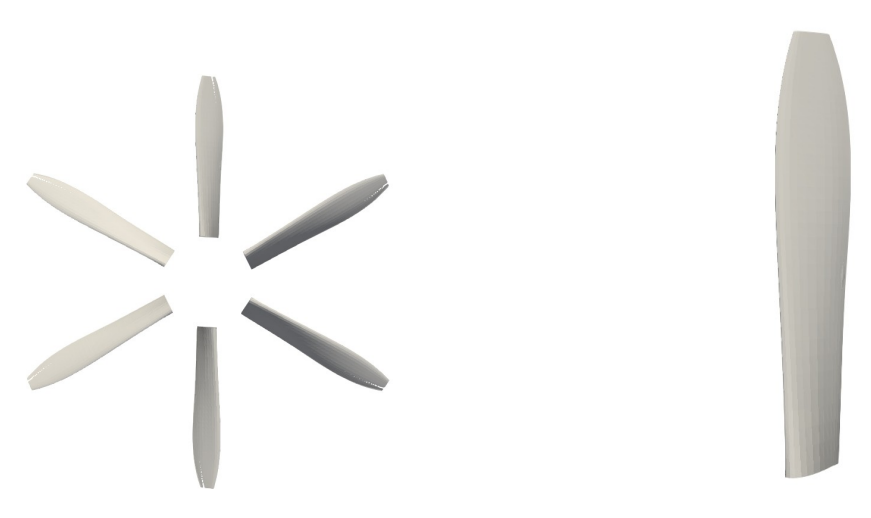
In this chapter, two different configurations are validated from both aerodynamic and aeroacoustic perspectives. The purpose of this section is to assess the capabilities of the coupling between FLOWUnsteady and the in-house aeroacoustic solver. First, the aerodynamic predictions of FLOWUnsteady are validated against available experimental and numerical data, seeking a balance between accuracy and computational cost. Next, the performance of the aeroacoustic solver is evaluated by validating noise directivity and spectra with numerical results. Finally, the results obtained for the isolated propeller and the distributed propeller are compared against both numerical and experimental data, in order to determine whether the solver can capture the unsteady interactions generated in this specific configuration.

5.1 Simulations Setup

The rotor selected for the validation is the TUD-XPROP-S 30, a six-bladed rotor with a diameter of 203.2 mm. At $r = 0.7R_{tip}$, the blade pitch angle is set to $\beta_{0.7R_{tip}} = 30^{\circ}$, while the corresponding chord length is $c_{0.7R_{tip}} = 15.5$ mm. The distributed configuration consists of three adjacent XPROP-S 30 rotors arranged with a tip-to-tip spacing of d/R = 0.04, as illustrated in Figure 5.2.

The inflow conditions are kept constant and uniform throughout the simulations: the inflow angle of attack is set to $\alpha_0 = 0^{\circ}$, and the inflow velocity is $30 \,\mathrm{m \, s^{-1}}$. Since FLOWUnsteady currently does not account for the presence of nacelles, these are excluded from the simulations, as shown in Figure 5.1. The freestream properties are defined as follows: density $\rho = 1.225 \,\mathrm{kg \, m^{-3}}$, dynamic viscosity $\mu = 1.225 \,\mathrm{kg \, m^{-3}}$, dynamic viscosity $\mu = 1.225 \,\mathrm{kg \, m^{-3}}$,

 $1.79 \times 10^{-5}\,\mathrm{kg\,m^{-1}\,s}$, and speed of sound $c_{\infty}=342.35\,\mathrm{m\,s^{-1}}$. To reproduce the zig-zag trip condition [9], the turbulent transition was imposed on the suction side of the airfoil at x/c=0.1 in the XFOIL polar calculation.



- (a) Frontal view of the TUD-XPROP-S.
- (b) Blade of TUD-XPROP-S.

Figure 5.1: Geometry of the isolated propeller TUD-XPROP-S.

In the simulations, viscosity effects were neglected, and Winckelmans's kernel was adopted with a core overlap factor of 1.3. To reduce computational cost in the aeroacoustic analyses, particles were canceled every ten time steps at a distance of five rotor diameters downstream of the rotor plane.

As reference, in figure 5.2 is reported the distributed configuration. In both simulations, the x axis is normal to the rotor plane and in the direction of the inflow. d/r is the tip-to-tip distance in the distributed configuration. The dashed line denotes the survey plane for the wake of both simulations.

The BEMT calculations were performed with the solver developed by Goyal [29]. The solver was fed with the polar generated by the wrapper integrated in FLOWUnsteady framework.

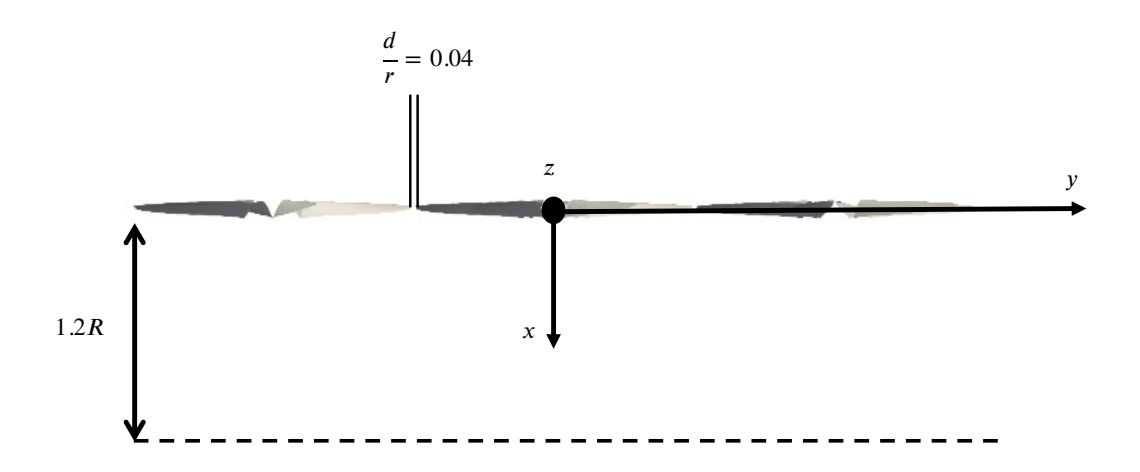


Figure 5.2: Distributed configuration. The dashed line indicates the wake survey plane.

5.2 Isolated Propeller

5.2.1 Aerodynamic Analysis

In this section, the performance of FLOWUnsteady is assessed by comparing its predictions with experimental data [30], BEMT calculations, and VLES numerical results [9]. The investigated advance ratio range extends from J = 0.80 to J = 1.35.

As a first step, the revolution convergence of the time-averaged integrated performance of the isolated XPROP-S-30 rotor was examined. As reported in Table 5.1, FLOWUnsteady achieved a relative error of 10^{-5} within three revolutions. The corresponding convergence trend during the iterations is illustrated in Figure 5.3a. Given the large number of simulations and the rapid convergence, only six revolutions were simulated. Moreover, in this analysis, 72 time steps per revolution were employed to reduce computational cost while preserving accuracy. The solver parameters are summarized in Table 5.2.

Figure 5.5 presents the averaged performance of the isolated-propeller configuration compared with experimental data and BEMT results. The thrust predictions from

Table 5.1: Number of revolutions required to reach convergence with a relative tolerance of 10^{-5} .

Parameter	Revolutions to convergence
T_C	2.65
Q_C	0.88
η	1.26

Table 5.2: Solver parameters for advance ratio analysis.

Parameter	Value
Blade elements	50
Revolutions	6
Particles per step	1
Number of particles	under 200.000
Time step per revolution	72
CPU time	8 CPU hours
Wall-Clock time	0.25 hours

both FLOWUnsteady and BEMT show good agreement with the experiments across the entire advance ratio range. The maximum absolute error is limited, with FLOWUnsteady reaching 6.15% and BEMT 5.65%. A similar trend is observed for the torque coefficient. In terms of propulsive efficiency, however, the discrepancy becomes more significant at higher advance ratios, where the error increases to 75.19% for FLOWUnsteady and 62.26% for BEMT. Despite this, both solvers predict comparable efficiency levels, suggesting that the discrepancy may be linked to the common set of airfoil polars used as input. The underestimation of thrust at high advance ratios by the solver appears to be the main source of error, likely due to limitations of XFOIL in predicting the aerodynamic coefficients of the blade airfoils [6].

Table 5.3: Absolute maximum errors for BEMT and FLOWUnsteady solvers.

Solver	T_c	Q_c	η
BEMT FLOWUnsteady			62.26%
TLOW Offsteady	0.1070	1.04/0	10.1970

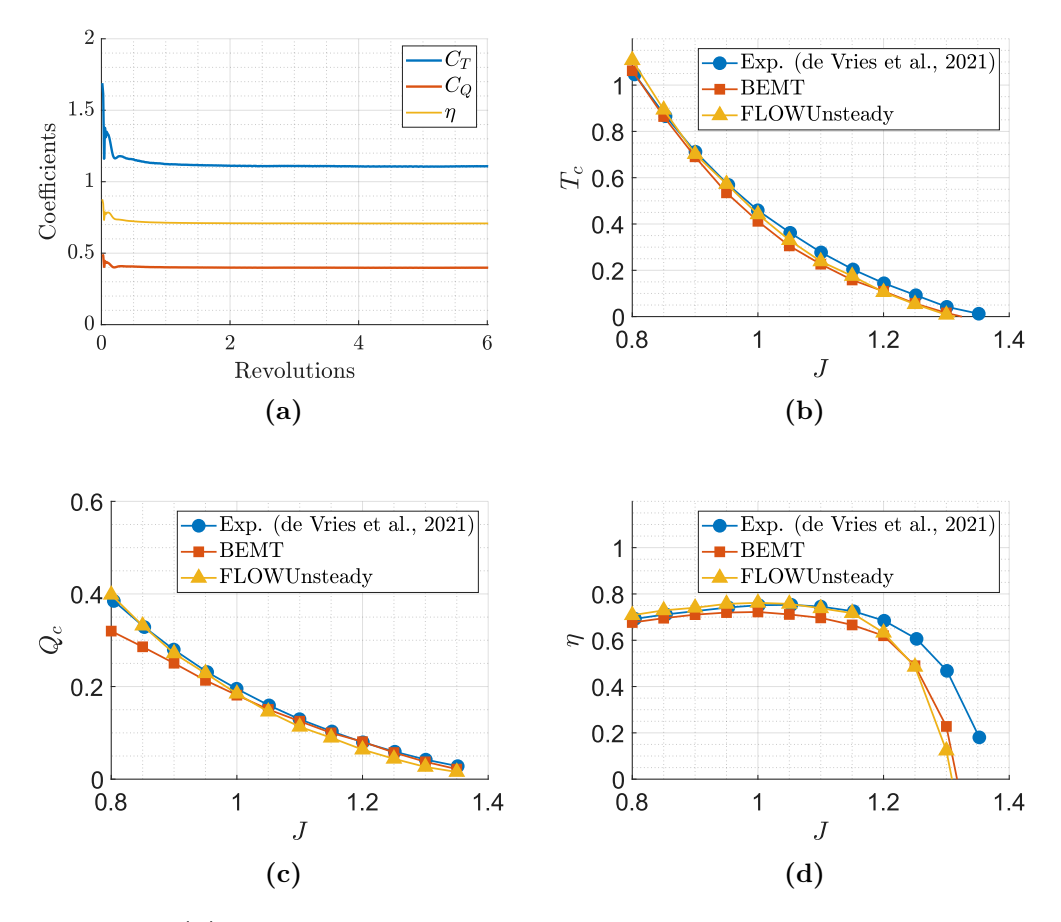


Figure 5.3: (a) Convergence of the three performance parameters. (b) FLOWUnsteady, BEMT and experimental thrust setting at different advance ratios. (c) FLOWUnsteady, BEMT and experimental torque coefficient at different advance ratios. (d) FLOWUnsteady, BEMT and experimental propulsive efficiency at different advance ratios.

To gain deeper insights into the rotor aerodynamics, the number of simulated revolutions and the time steps per revolution were increased for the case at J=0.80. This advance ratio was selected to allow direct comparison with the results reported in [9]. Moreover, the number of time steps per revolution was set to 180 in order to match the temporal resolution of the simulations of the same reference. The solver parameters are summarized in Table 5.4.

The thrust loading profile predicted by FLOWUnsteady at J=0.80 tends to overestimate the blade loading, as also evident from the integrated values shown in Figure 5.5. BEMT results provide a closer match to the VLES thrust profile;

Table 5.4: Solver parameters for detailed analysis.

Parameter	Value
Blade elements	50
Revolutions	25
Particles per step	1
Number of particles	under 280.000
Time step per revolution	180
CPU time	240 CPU hours
Wall-Clock time	7.5 hours

however, they still exhibit a peak of comparable magnitude to that predicted by FLOWUnsteady. This similarity can be attributed to the common airfoil polars employed. The FLOWUnsteady profile displays a different trend near the hub region, which could be related to inaccuracies in the hub—tip correction parameters. Nevertheless, the radial location of the peak predicted by FLOWUnsteady shows better agreement with VLES compared to BEMT. These observations are consistent with the findings of Goyal et al. [6]. The difference in the peak position between BEMT and FLOWUnsteady likely stems from wake resolution effects, as BEMT does not account for momentum swirl and wake contraction or other tip effects [6]. The values are summarized in table 5.5

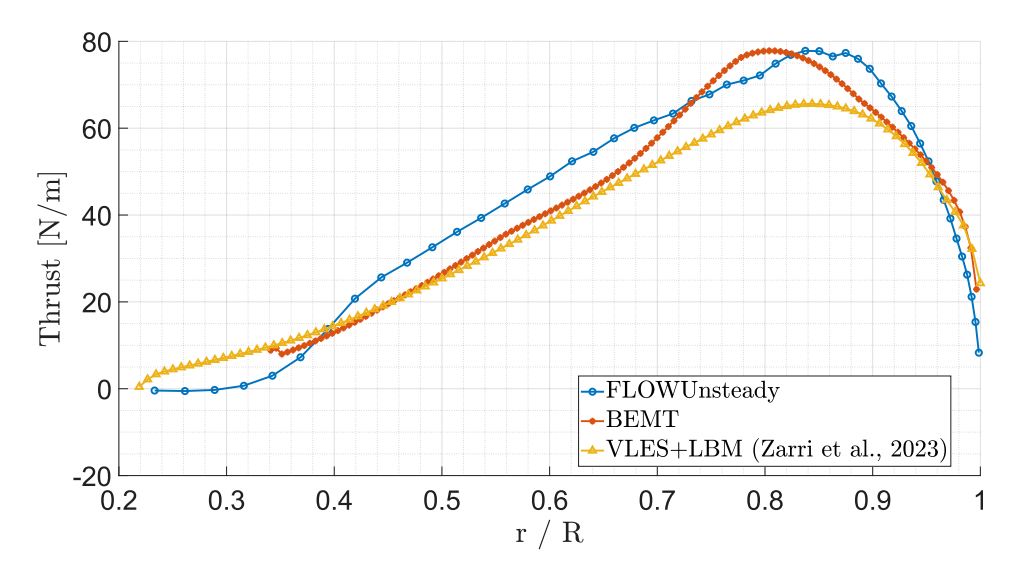


Figure 5.4: Blade Loading comparison of the three solvers with both FLOWUnsteady tripped and no-tripped solution.

Table 5.5: Peak thrust distribution values and their corresponding radial positions.

Method	Peak Thrust [N/m]	r/R at Peak
FLOWUnsteady	77.8131	0.8375
BEMT	77.8204	0.8039
VLES+LBM (Zarri et al., 2023)	65.5976	0.8438

Figure 5.5b shows the axial velocity comparison. The FLOWUnsteady predictions follow a similar trend across the solutions, but consistently overestimate the values, in agreement with the overprediction observed in the thrust loading results. At the blade tip, the axial velocity exhibits a behavior similar to that reported by Alvarez [8] in his convergence study, where increasing the particles shed per revolution improved the resolution of the tip vortex and, consequently, the velocity profile. In the present case, a higher number of particles per revolution is therefore required to achieve a more accurate resolution of the vortex structures near the tip.

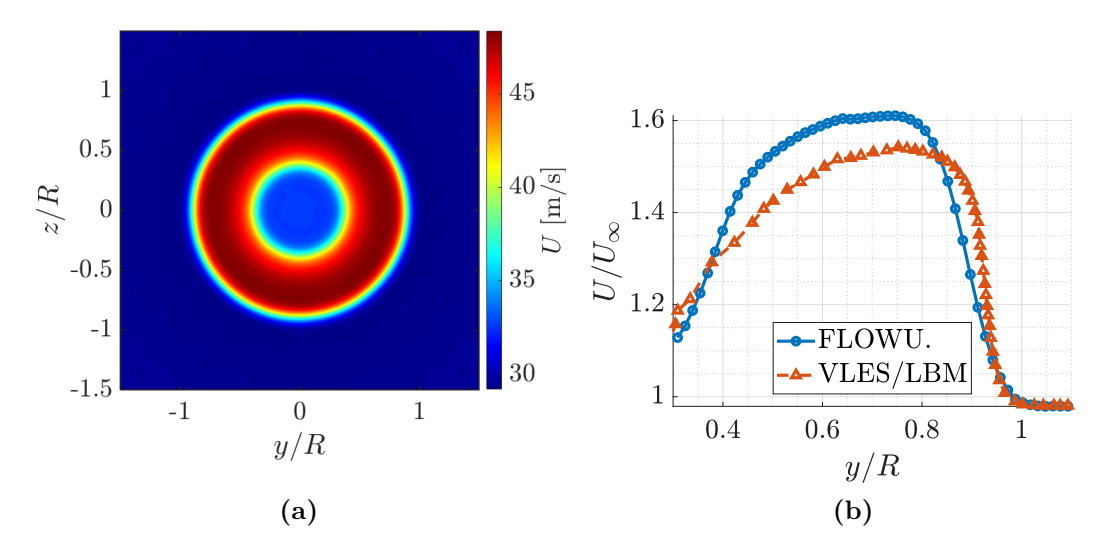


Figure 5.5: (a) Phase-locked velocity magnitude in the survey plane of the FLOWUnsteady tripped simulation. (b) Comparison of the normalized axial velocity of the FLOWUnsteady tripped, no.tripped solution and the VLES solution.

5.2.2 Aeroacoustics Analysis

In this section, both tonal and broadband noise predictions for the isolated propeller are analyzed. Following Reference [9], the acoustic data is sampled at 33218 Hz and the tripped solution is used. The observer is positioned at a distance of r=10D from the propeller center. The Power Spectral Density (PSD) is computed using Welch's method and filtered with a Hanning window, corresponding to a bandwidth of $\Delta f = 97.34$ Hz. The far-field PSD is defined as:

$$S_{pp}(f) = 10\log_{10}\left(\frac{PSD(f)}{p_{ref}^2}\right)$$

where $p_{ref} = 20 \,\mu\text{Pa}$ is the reference pressure. The Sound Pressure Level (SPL) and Overall Sound Pressure Level are computed as:

$$SPL(f) = 10 \log_{10} \left(\frac{\Delta f PSD(f)}{p_{ref}^2} \right), \quad OASPL = 10 \log_{10} \left(\frac{1}{p_{ref}^2} \int_{f_{min}}^{f_{max}} PSD(f) df \right)$$

Figure 5.6 illustrates the directivity of the first Blade Passing Frequency (BPF) of the tonal noise, computed in the XZ plane. The upstream and downstream directions correspond to 180° and 0° , respectively. The results show good agreement with VLES/LBM simulations, capturing unsteady behavior in both directions. On the rotor plane, FLOWUnsteady accurately predicts the PSD associated with thickness and steady loading noise. Additionally, FLOWUnsteady captures the unsteady fluctuations along the axis of rotation, albeit with slightly higher amplitudes compared to VLES/LBM, likely due to the lower dissipation characteristic of the Vortex Particle Method (VPM).

Figure 5.7a presents the PSD in the rotor plane of the isolated propeller. The first Blade Passing Frequency (BPF) is well predicted, while higher harmonics are not accurately captured. These visible higher harmonics are likely due to the low numerical dissipation of the Vortex Particle Method (VPM) solver. Figure 5.7b shows the PSD along the propeller's axis of rotation. Neither solver predicts tonal peaks at BPF in this direction, consistent with propeller noise theory [31], but both display broadband content arising from unsteady fluctuations. The overprediction at low frequencies, also attributable to the low dissipation of the VPM, is evident, as the in-house solver predicts higher PSD levels. At high frequencies, the broadband content is not captured in any direction, as this portion of the spectrum is modeled by the tonal module of the in-house solver. The VLES/LBM solver exhibits errors in tonal content at frequencies below the first BPF due to the computational grid, an issue not present in the coupled solver. Despite the missing higher harmonics, the coupled solver accurately predicts the first BPF, with a deviation of 1.16 dB

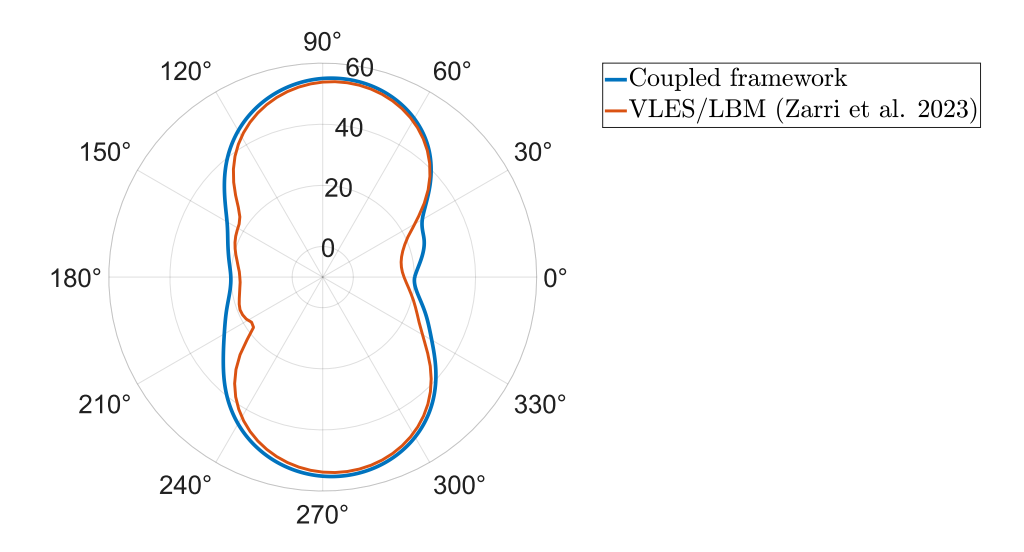


Figure 5.6: SPL directivity of the first BPF of the isolated rotor on XZ plane.

and 2.50 dB in the rotor plane and along the rotation axis respectively.

For the broadband noise analyses, several combinations of Wall Pressure Fluctuation functions were explored in order to find the better one. The analyses were conducted only for the upstream direction, in which the broadband content is dominant due to unsteady fluctuation. The Corcos model is kept as default with b = 1, $\alpha' = 0.9$ and the boundary layer's parameters are extracted at x/c = 0.99.

Figure 5.8 presents the trailing-edge noise of the isolated propeller obtained using different WPF functions. The broadband module was fed with the effective velocity and effective angle of attack computed by FLOWUnsteady. The data were post-processed with a phase-locked approach in order to take into account the unsteadiness during the revolution. The best agreement with the VLES data is achieved with Rozenberg on the Suction Side (SS) and Kamruzzaman on the Pressure Side (PS). This outcome can be explained by the underlying formulations: Kamruzzaman's model is derived from measurements in both zero and adverse pressure gradient flows, while Rozenberg's is specifically developed for adverse pressure gradients, which is consistent with the typical aerodynamic loading on a propeller blade. When Rozenberg is applied on the PS, the prediction remains reasonably accurate, although some discrepancies arise at low frequencies. This behavior may be attributed to the fact that the PS flow is predominantly governed by an adverse pressure gradient [7], which is not represented in Rozenberg's formulation.

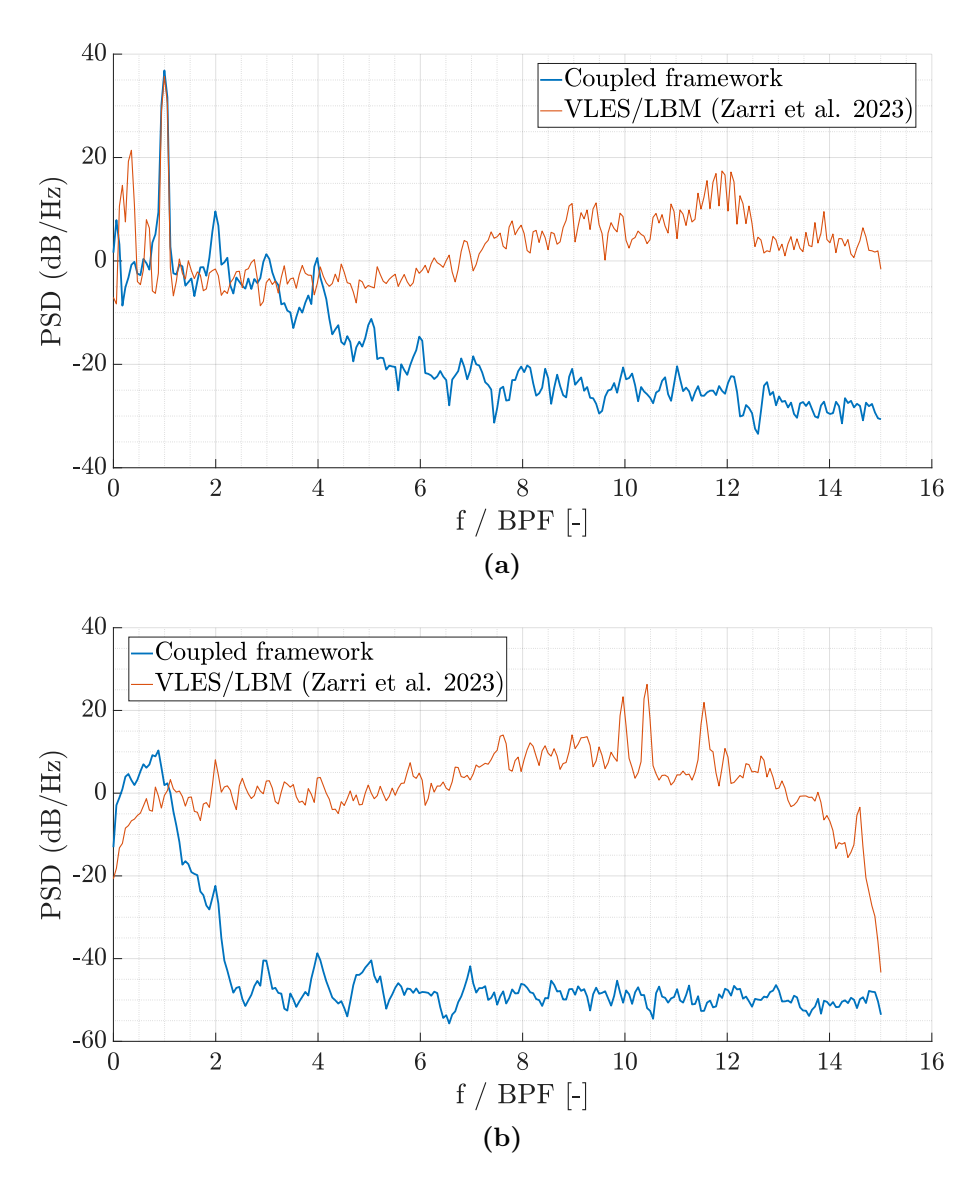


Figure 5.7: (a) Power Spectral Density of the tonal signal of the isolated propeller in the rotor plane. (b) Power Spectral Density of the tonal signal of the isolated propeller in the rotation axis.

Nevertheless, it is worth noting that the other WPF models also provide a fairly good agreement with the numerical results.

Figure 5.9 shows the combined spectrum obtained by summing the tonal and broadband contributions with Rozenberg's model for the SS and Kamruzzaman's model for the PS. The results exhibit good agreement with the VLES/LBM

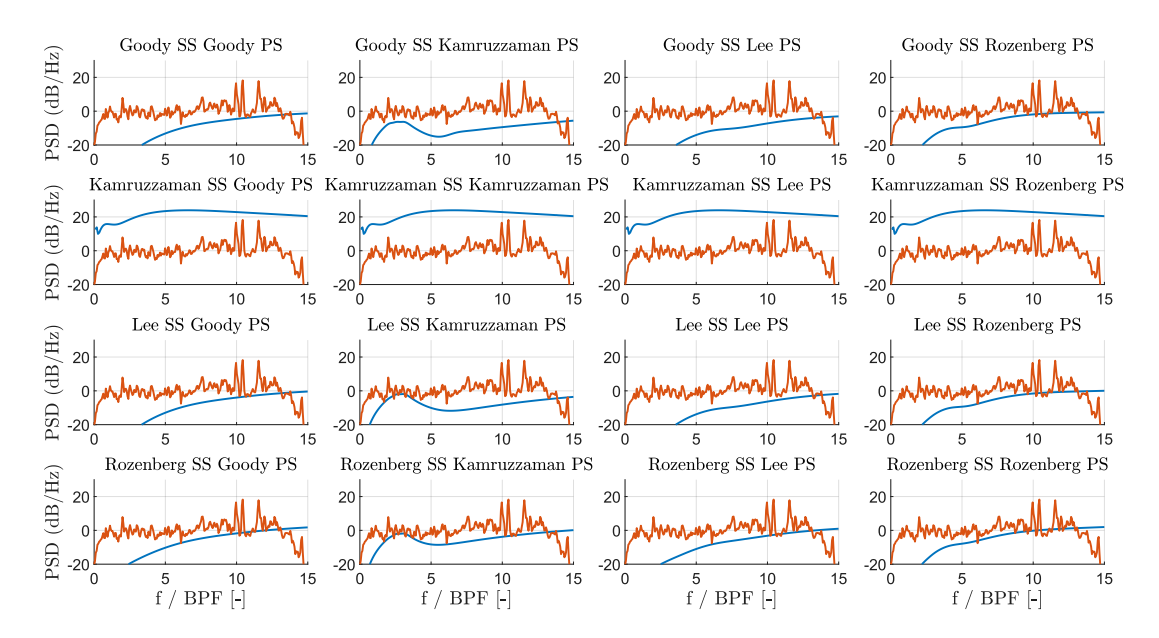


Figure 5.8: Broadband analyses at different WPF functions for the isolated propeller.

prediction, although the tonal component tends to slightly overpredict, while the broadband contribution is slightly underpredicted. Nevertheless, the Overall Sound Pressure Level (OASPL) matches well with the VLES/LBM reference. The OASPL predicted by the coupled framework is $40.43\,\mathrm{dB}$, which differs by $5.35\,\mathrm{dB}$ from the VLES reference value of $45.78\,\mathrm{dB}$.

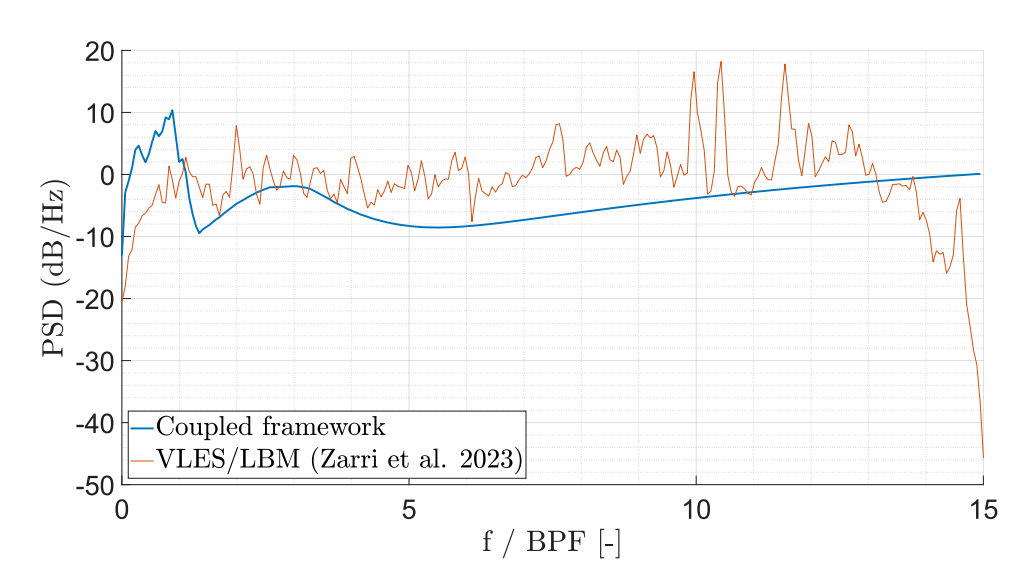


Figure 5.9: Predicted sprectrum for the isolated propeller.

5.3 Distributed Propellers

For the distributed propulsion analyses, the same parameters used in the isolated propeller simulation are utilized.

5.3.1 Convergence Analysis

For the distributed configuration, no convergence data are available in the literature. Therefore, a convergence analysis was performed considering the following parameters: number of time steps per revolution N_{steps} , number of sheds per revolution N_{shed} , and number of blade elements N_{el} . It should be noted that temporal and spatial convergence are coupled. To decouple them, the procedure suggested by Alvarez [8] was adopted. The metric used for the analysis was the thrust coefficient T_C . Three simulations per parameter were carried out, and the results were fitted with a function of the form $T_C = (T_C)_{extr} + \frac{b}{N_i^p}$, where p is the convergence's order. T_C was computed as the mean of the thrust setting of the three propellers.

Figure 5.10a shows the convergence as a function of the number of blade elements, ranging from 15 to 50. A non-monotonic behavior is observed, consistent with the findings of Alvarez for the isolated propeller. This behavior may be attributed to numerical noise introduced by the spline used to generate the blade geometry. The error relative to the extrapolated finest solution is 4.66%, corresponding to an approximate order of accuracy of $p \simeq 1$.

Figure 5.10b presents the convergence as a function of N_{shed} , which exhibits a monotonic behavior. For the finest solution, the associated error is 6%, with a low order of accuracy of $p \simeq 0.4$.

Figure 5.10c shows the convergence as a function of N_{steps} , which also displays monotonic behavior. The error associated with the finest solution is 8.46%, corresponding to an order of accuracy of $p \simeq 0.267$. These results indicate that additional simulations with higher resolution are required to perform a more accurate analysis of the convergence order.

5.3.2 Aerodynamic Analysis

In this section, the aerodynamics of the distributed propeller configuration are investigated. First, the aerodynamic performance at different advance ratios is analyzed and compared with the isolated propeller results. Then, a more detailed

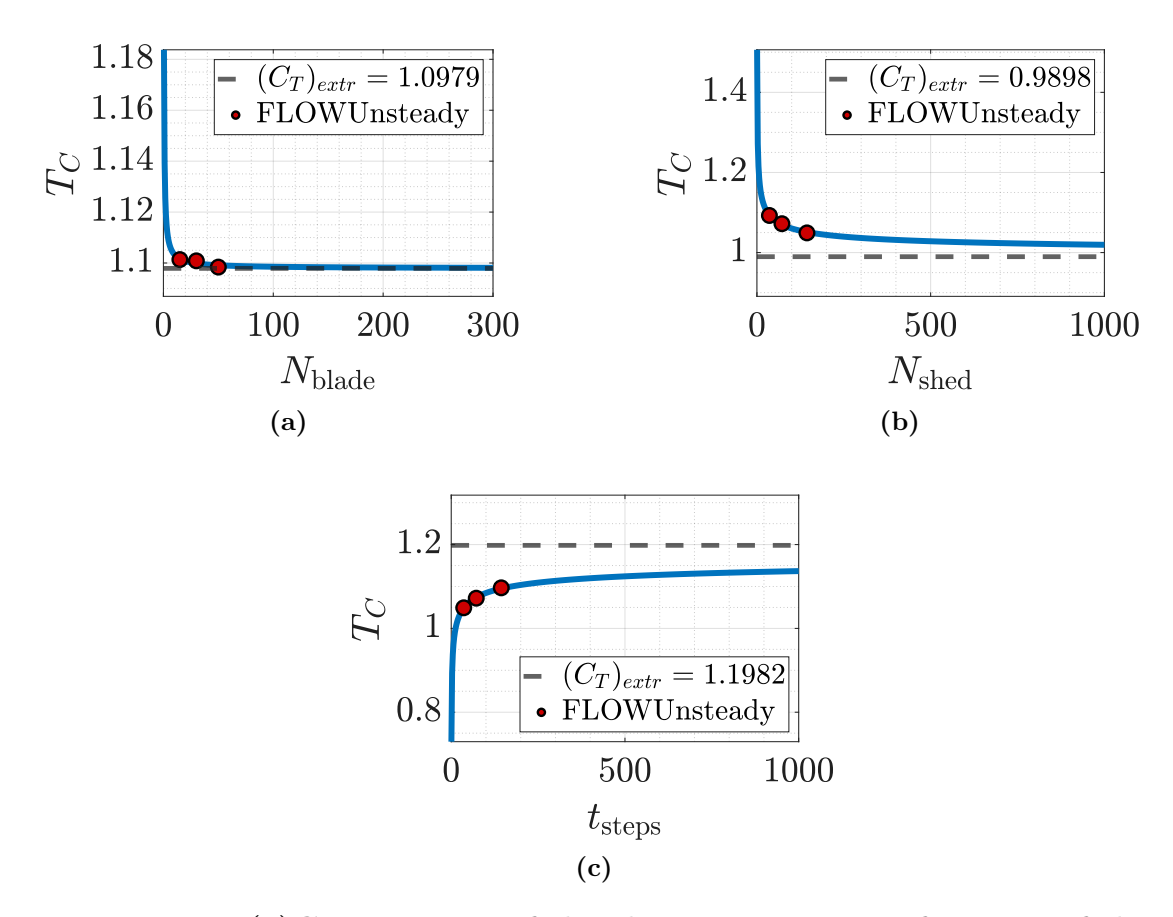


Figure 5.10: (a) Convergence of the thrust setting as a function of the number of blade elements. (b) Convergence of the thrust setting as a function of the number of shed particles.(c) Convergence of the thrust setting as a function of the number of time steps.

analysis is carried out to examine if the coupled framework is able to capture the aerodynamic interactions present in this configuration. The number of time steps per revolution and the number of revolutions are kept the same as in the isolated case, owing to the rapid convergence of the aerodynamic parameters. Table 5.6 reports the convergence results. However, it should be noted that the relative error is higher in this case, as the solution never decreases below 10^{-5} . In the table 5.7 are shown the solver parameters and the computational cost.

Table 5.7 summarizes the solver parameters adopted in the simulations. Figure 5.11 compares the aerodynamic performance of the isolated propeller with that of the central propeller in the distributed configuration. As can be seen, aerodynamic interference does not significantly affect the time-averaged performance of the

Table 5.6: Number of revolutions required to reach convergence with a relative tolerance of $3 \cdot 10^{-5}$.

Parameter	Revolutions to convergence
$\overline{T_C}$	2.32
Q_C	0.32
η	2.17

Table 5.7: Solver parameters for advance ratio analysis of the distributed configuration.

Parameter	Value
Blade elements	50
Revolutions	6
Particles per step	1
Number of particles	under 610.000
Time step per revolution	72
CPU time	30 CPU hours
Wall-Clock time	0.94 hours

propeller. To further investigate these findings, the simulation resolution was increased, as summarized in Table 5.8.

Table 5.8: Solver parameters for advance ratio analysis of the distributed configuration.

Parameter	Value
Blade elements	50
Revolutions	25
Particles per step	1
Number of particles	under 865.000
Time step per revolution	180
CPU time	834.13 CPU hours
Wall-Clock time	26.1 hours

Figure 5.12 shows the unsteady fluctuations of the distributed configuration in comparison with the isolated case. A more detailed analysis reveals that the central rotor has a slightly lower mean thrust than both the isolated and the lateral rotors. However, the fluctuations of the central rotor are about twice those observed for

the lateral ones, with deviations from the mean of 0.56% and 0.28%, respectively. These results confirm that, although the mean performance in the distributed configuration is not significantly altered, the unsteady fluctuations are amplified compared with the isolated case. All these findings are consistent with the results reported in Reference [9], although the mean values tend to be overpredicted, as already observed for the isolated case.

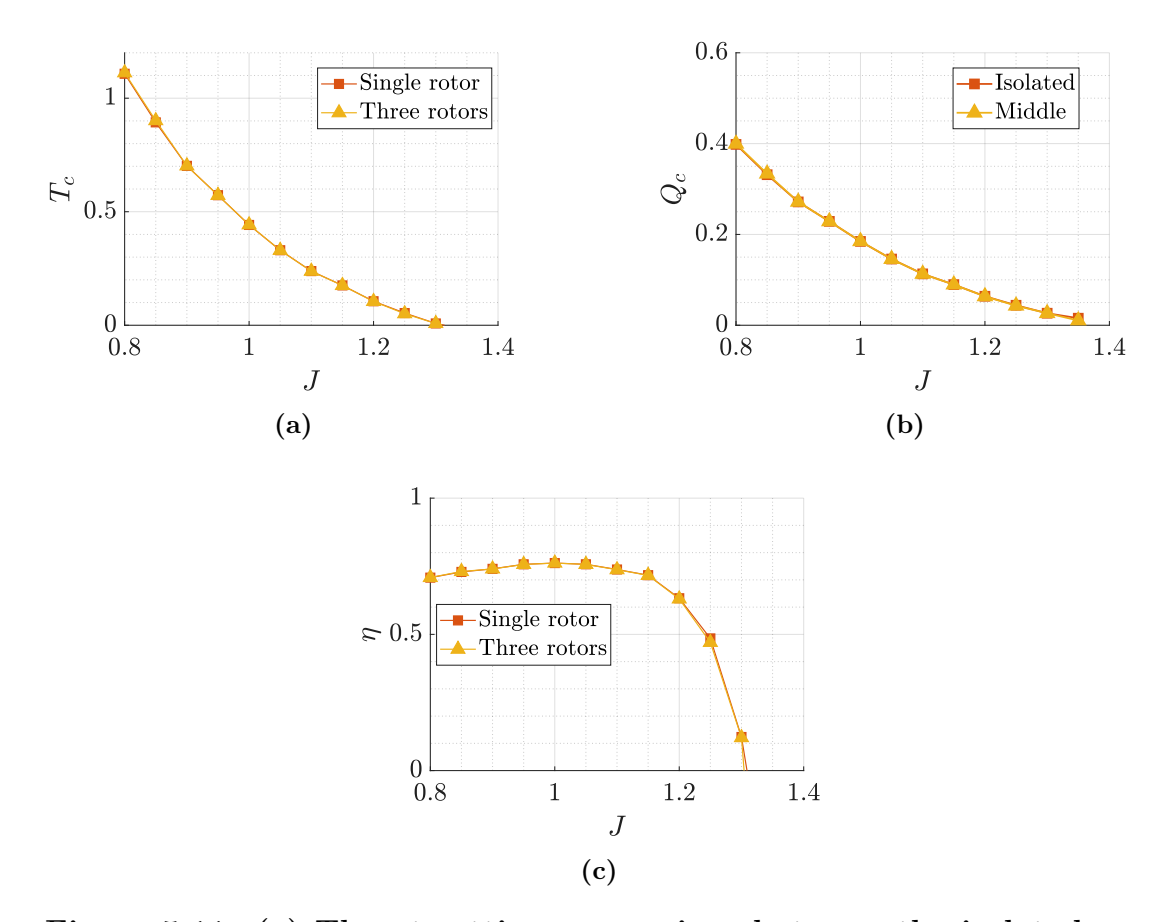


Figure 5.11: (a) Thrust setting comparison between the isolated propeller and the middle one in the distributed configuration. (b) Torque coefficient comparison between the isolated propeller and the middle one in the distributed configuration.(c) Propulsive efficiency setting comparison between the isolated propeller and the middle one in the distributed configuration.

Figure 5.13b shows the phase-locked thrust difference between the central propeller and the isolated one. The interaction physics are consistent with the findings of

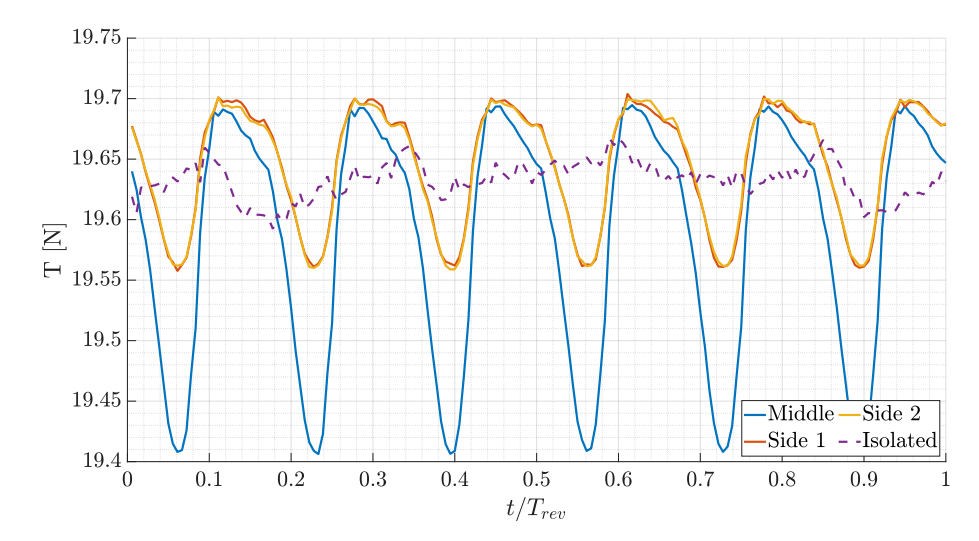


Figure 5.12: Comparison of the time history of the thrust of each propeller.

References [9] and [5]. In particular, the central propeller experiences a reduction in thrust as its blade approaches an adjacent propeller, followed by a subsequent increase. As noted in Reference [5], this effect would be symmetric and therefore does not significantly affect the time-averaged thrust. However, examining Figure 5.12, it can be observed that this symmetry is lost for the central propeller, a feature not evident in the phase-locked plot. This behavior is due to a reduction in the averaged thrust of the central propeller, which appears to be overpredicted with respect to the VLES results. The averaged normalized thrust is $T_{middle}/T_{iso} \simeq 99.6$. This value is similar to the one obtained by Alvare et al. in Reference [32]. Moreover, when compared to the findings of Reference [9], FLOWUnsteady seems to overestimate the amplitude of the thrust fluctuations on the rotor.

Figure 5.13a presents the phase-locked difference in thrust for the lateral propeller compared to the isolated case. In this scenario, the lateral propeller reduces its thrust when the blade approaches the tip of the adjacent propeller's blade. It is important to note that this occurs once per revolution, whereas for the central propeller, the interaction occurs twice per revolution. The magnitude of the difference is larger than that reported by Zarri et al. [9], which can be attributed to their study considering a configuration with blades phased differently, resulting in reduced unsteady interactions.

Figure 5.14 depicts the vortex structure in the wake of the middle propeller. The figure shows that the vortices persist behind the rotor without merging, consistent

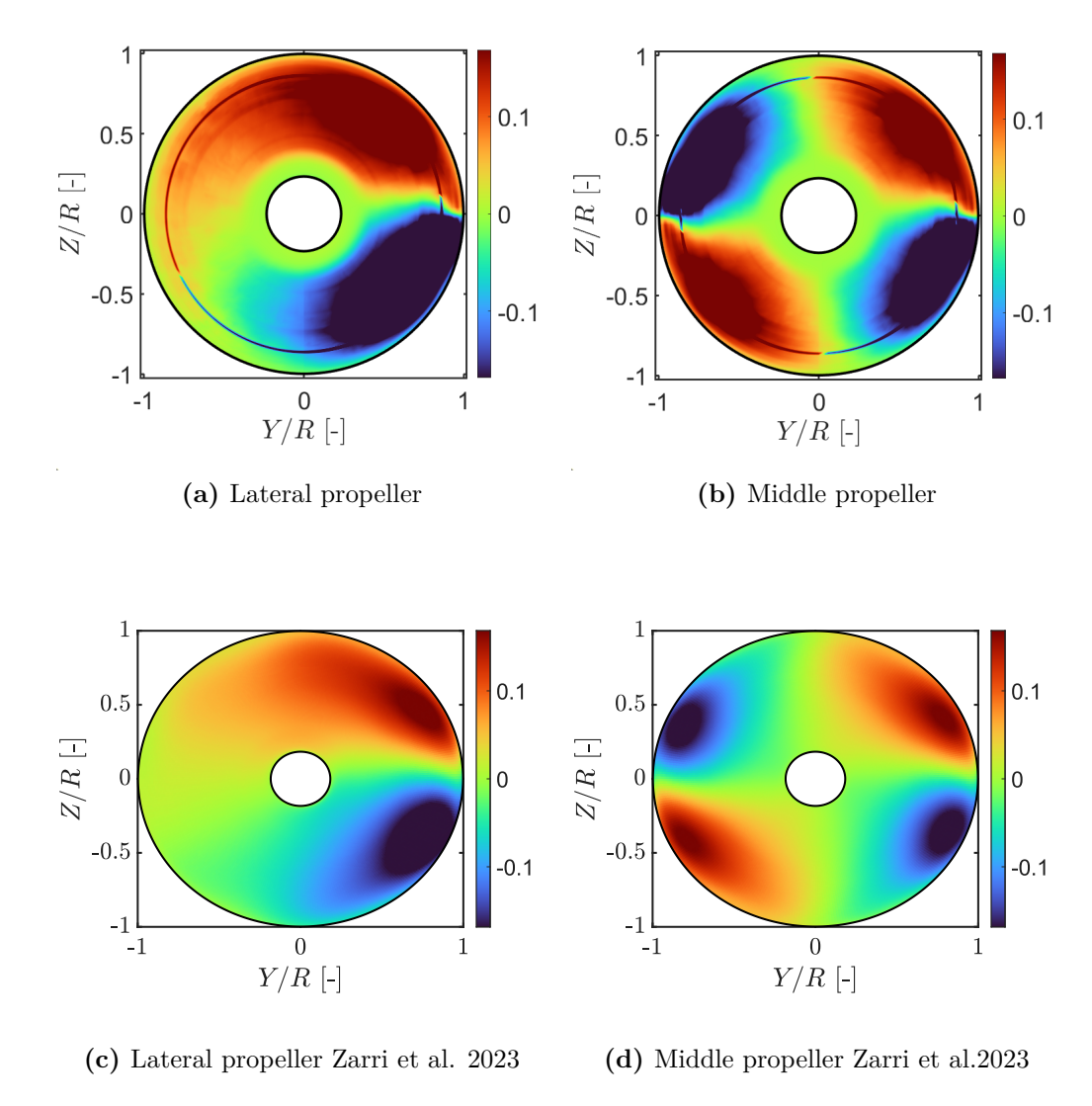


Figure 5.13: Phase-locked thrust setting difference between propellers of the distributed configuration and the isolated propeller. Comparison with result in Reference [9],

with the experimental observations by de Vries et al. [30] and the numerical results of Zarri et al. [9]. A similar trend is observed in the slipstream evolution: FLOWUnsteady also predicts that the vortex structure is deformed due to the proximity of the adjacent propellers.

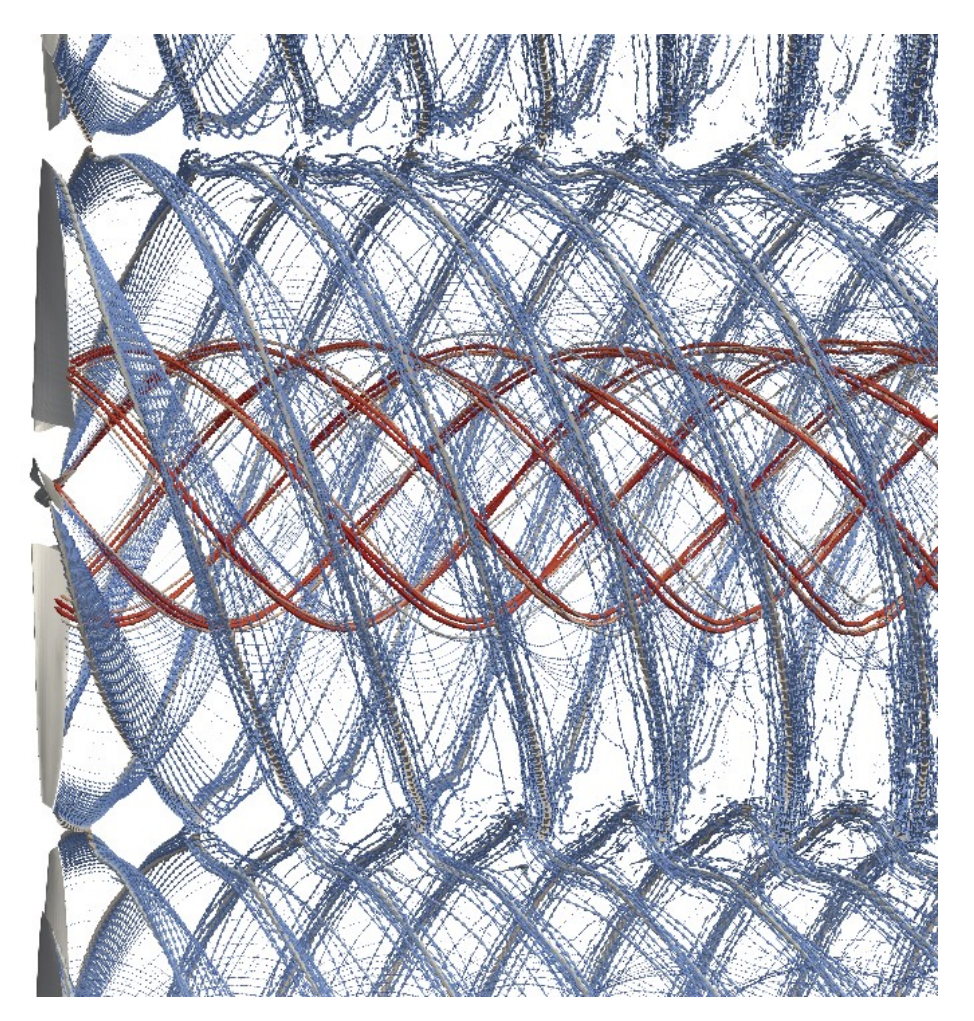


Figure 5.14: Vortex structure of the middle propeller of the distributed configuration.

Figure 5.15a reports the normalized axial velocity. Overall, the prediction is satisfactory; however, due to the relatively low number of blade elements, the tip vortices are not accurately captured [8]. Figure 5.15b shows the time-averaged velocity magnitude at 1.2R downstream of the rotors. The characteristic deformation induced by the proximity of adjacent rotors is clearly visible. Although the solution is not fully refined, the physical trends are correctly reproduced, as also observed in References [9] and [30]. In particular, the distributed configuration exhibits a symmetric pattern near y/R=1.04, corresponding to the distance between the propellers. The induced field from the side propellers reduces the maximum velocity and enlarges the wake, capturing the expected aerodynamic interactions.

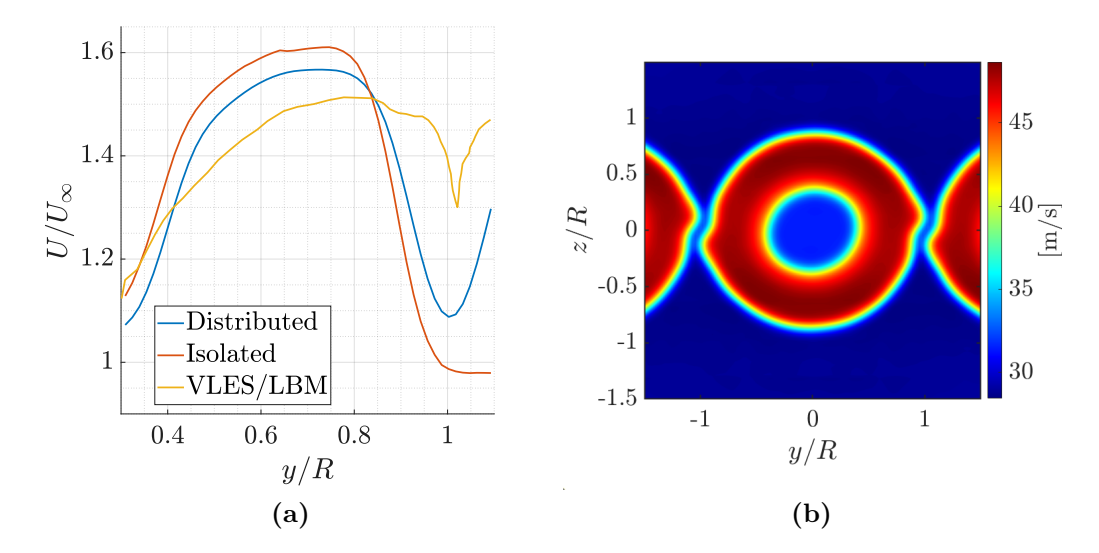


Figure 5.15: (a) Comparison of the normalized axial velocity with the VLES results in Reference [9] and the isolated case. (b) Averaged magnitude velocity in a plane 1.2R downstream from the propeller.

5.3.3 Aeroacoustic Analysis

In this section, the performance of the coupled framework is explored on predicting tonal and broadband noise of a distributed configuration. The results will be compared with the VLES/LBM results in Reference [9]. The acoustic analyses were conducted with the same parameters as the isolated case.

Figure 5.16 shows the directivity in the XZ plane of the first BPF for the middle rotor in the distributed configuration. The results are in good agreement with the VLES/LBM simulations, capturing the noise generated by the unsteady interaction of the propellers. The directivity is accurately predicted in the region close to the rotor plane, where the steady loading noise and thickness noise are dominant, while small discrepancies appear near the axis of rotation, where the unsteady fluctuations are dominant. These differences can be attributed to the unresolved tip vortices. The maximum error occurs at 30° and 60°, with a value of 19.56 dB.

Figures 5.17a and 5.17b present the PSD on the rotor plane and along the rotation axis, respectively. On the rotor plane, the coupled framework predicts the spectrum up to the third BPF with an error of 5.6 dB/Hz. Along the rotation axis, the first BPF is well captured, whereas the higher harmonics exhibit larger errors. Nevertheless, the presence of tonal peaks can still be observed, indicating that the

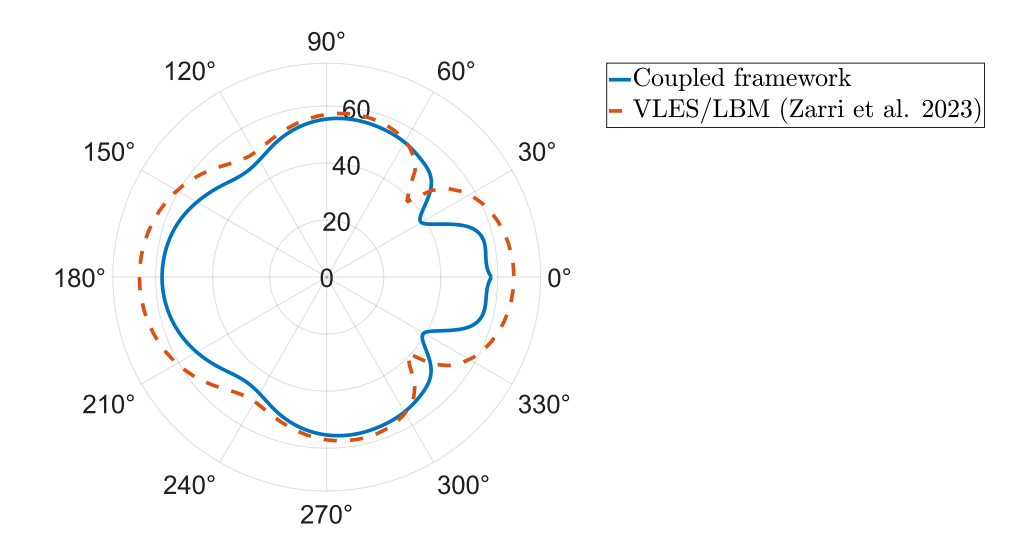


Figure 5.16: Directivity of the first BPF of the middle rotor.

spectrum is no longer purely broadband. These tonal components are also present in the VLES results and have been attributed to the tip-on-tip interaction observed in the aerodynamic analysis [9].

Figure 5.18 shows the trailing-edge noise of the middle propeller obtained with different WPF functions for an observer located along the rotation axis. Rozenberg for the suction side (SS) and Kamruzzaman for the pressure side (PS) again provide the best agreement, even in the distributed configuration. This outcome is consistent with the previous aerodynamic results, where FLOWUnsteady did not predict significant changes in the aerodynamic performance. Similarly, the overall broadband noise from the VLES/LBM simulations [9] does not exhibit substantial variations, supporting the predictions of the coupled framework. The OASPL predicted by VLES/LBM is 67.45 dB, while the coupled framework yields 64.79 dB, corresponding to a deviation of 2.66 dB. Figure 5.19 presents the combined tonal and broadband spectra for an observer on the rotation axis. The broadband component is calculated with Rozenberg for the SS and Kamruzzaman for the PS.

A deeper analysis of the acoustic pressure predicted by the tonal module is reported. As shown in figures 5.20a and 5.20b, the acoustic pressure measured in the rotor plane follows a sinusoidal trend consistent with the VLES/LBM solution [9]. However, some high-frequency oscillations are not captured, which is likely related to unresolved tip vortices or turbulent phenomena in the wake. Along the rotation axis, as shown in figures 5.20c and 5.20d, the time history does not reproduce either the absolute pressure level or the amplitude of the oscillations,

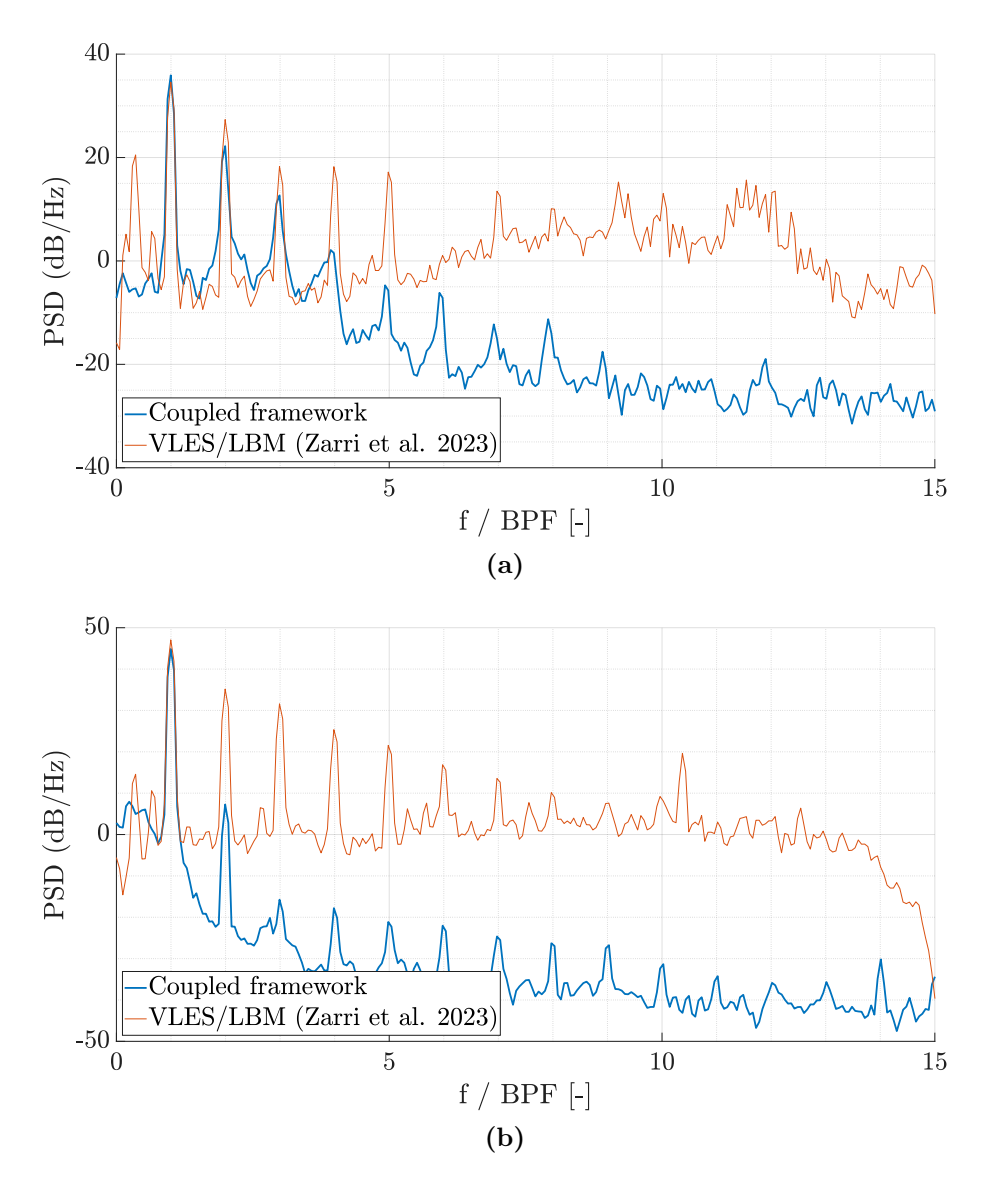


Figure 5.17: (a) Power Spectral Density of the tonal signal of the middle propeller in the rotor plane. (b) Power Spectral Density of the tonal signal of the middle propeller in the rotation axis.

and it also fails to capture the high-frequency content. This explains why, although the framework correctly predicts the increase in emitted noise with respect to the isolated case, it underestimates the SPL along the axis. In this direction, the dominant noise-generation mechanism is the unsteady loading induced by the tip-on-tip interaction [9]. Therefore, a finer spatial resolution could improve the prediction of both high-frequency oscillations and overall magnitude. It should also be noted

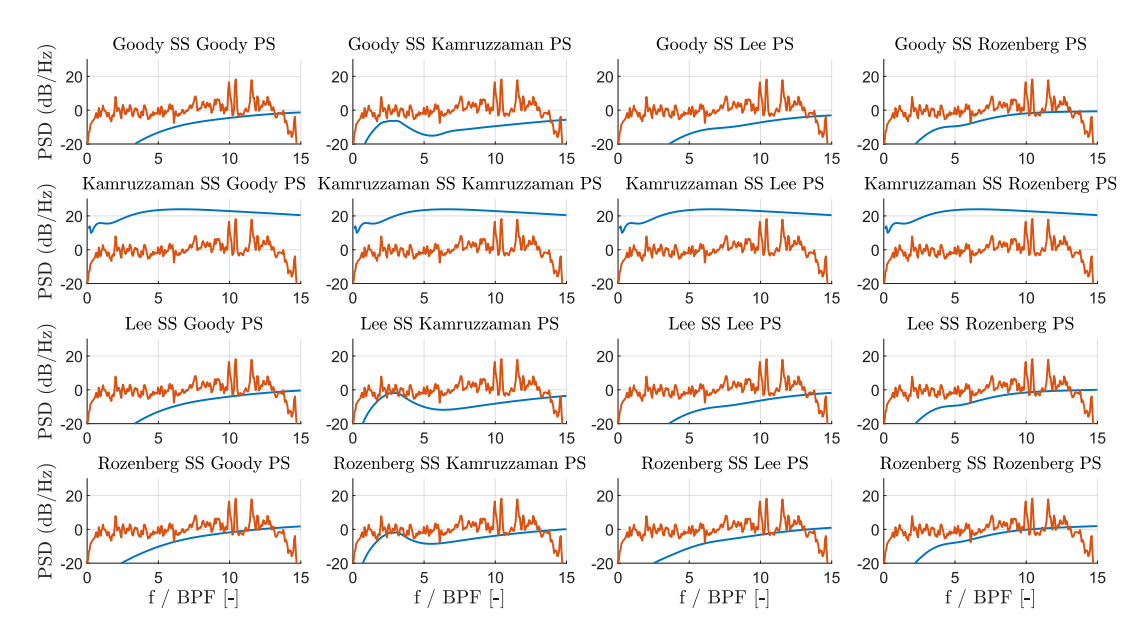


Figure 5.18: Broadband analyses at different WPF functions for the middle propeller of the distributed configuration with an observer placed in the rotation axis.

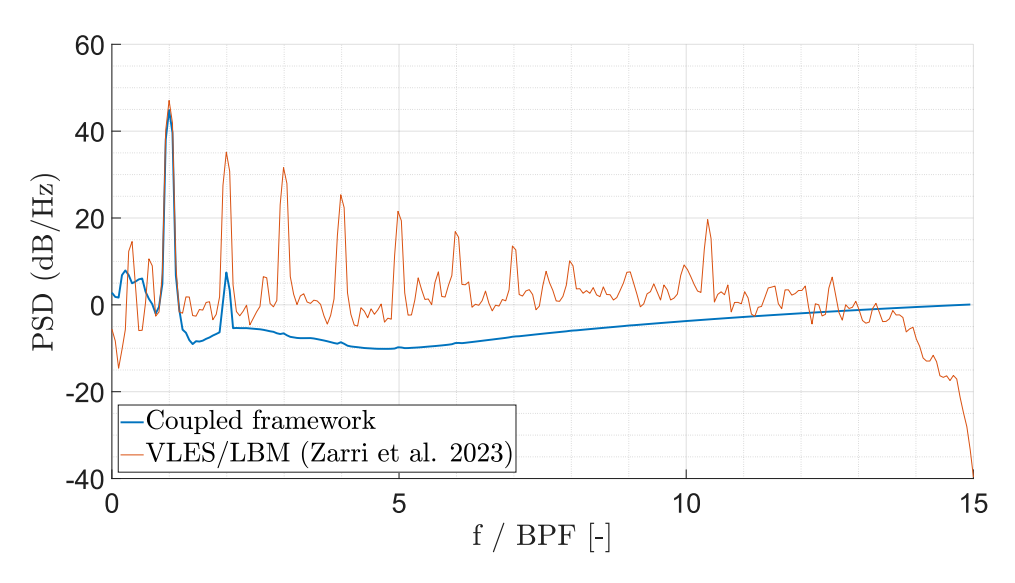


Figure 5.19: Predicted sprectrum for the middle propeller of the distributed configuration with an observer placed on the rotation axis.

that the nacelles are not modeled in the present configuration; therefore, possible rotor—nacelle interactions are not captured, which may contribute to discrepancies

with the reference data.

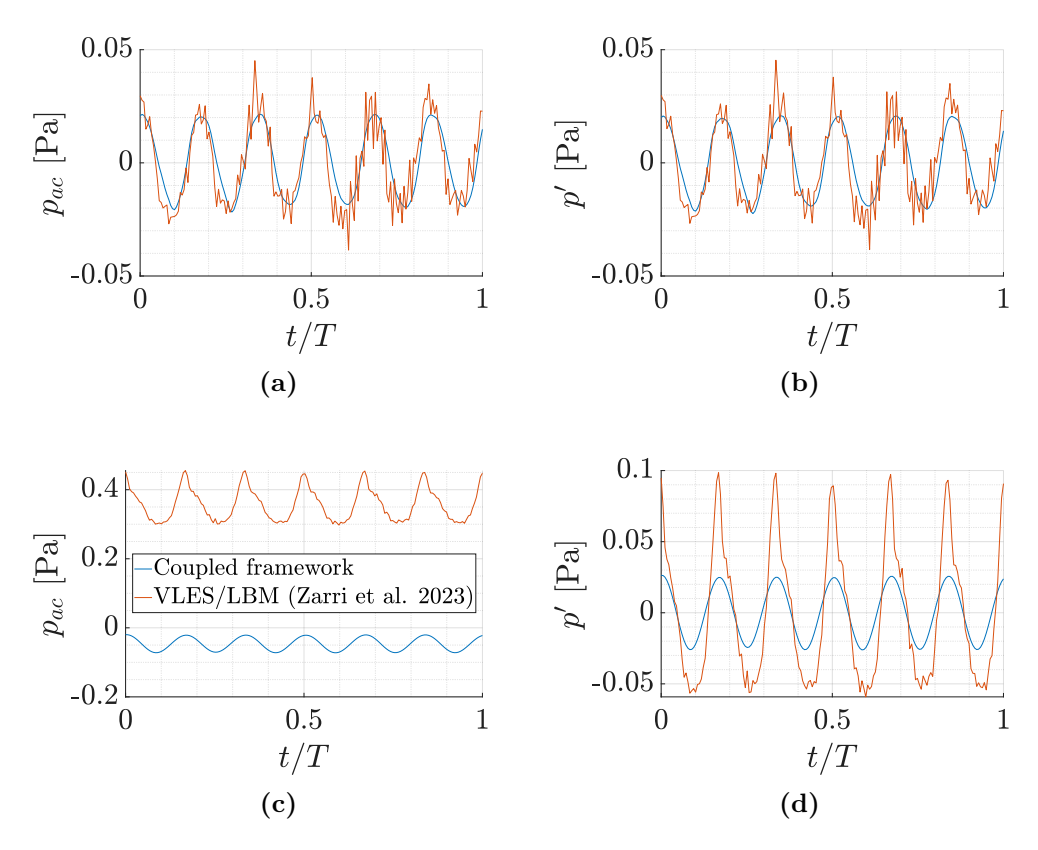


Figure 5.20: (a) Acoustic pressure on the rotor plane. (b) Acoustic pressure fluctuation on the rotor plane. (c) Acoustic pressure on the rotation axis. (d) Acoustic pressure fluctuation on the rotation axis.

Figure 5.22 compares the trailing-edge noise emitted by the middle propeller with that of the isolated configuration. It can be observed that the high-frequency spectrum is not influenced by the propeller arrangement, as both curves follow the same trend and exhibit similar magnitudes. A similar behavior is also visible in the very low-frequency region. Slight differences appear in the mid-low frequency range, where a noticeable jump is present. However, this difference disappears when other WPF functions are considered. In fact, the comparison of the trailing-edge noise with different WPF functions, also reported in figure 5.22, shows that the broadband content remains largely unchanged, especially at high frequencies. Kamruzzaman applied to the SS generates a pronounced peak at low frequencies, whereas on the PS, when combined with other WPF functions, it reduces the peak level. The physical explanation for this behavior requires further investigation with

high-fidelity numerical tools. Due to the fact that trailing-edge noise for a propeller is more evident at high frequencies, these results suggest that it is possible to study the trailing-edge noise of a propeller in a distributed configuration starting from the isolated configuration. However, these results need to be confirmed by additional simulations with higher spatial and temporal resolution.

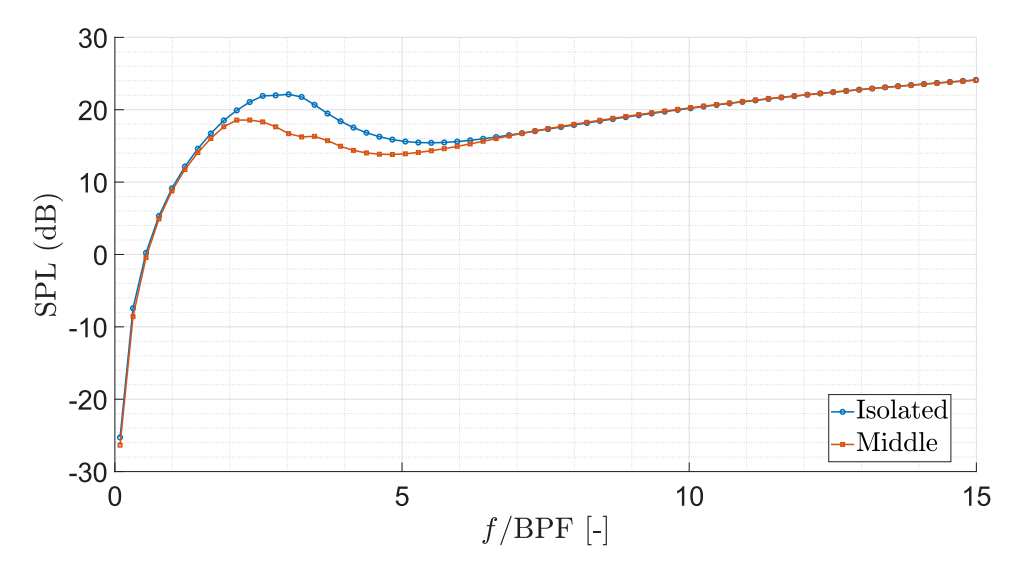


Figure 5.21: Comparison of the trailing edge noise emission on the rotation axis.

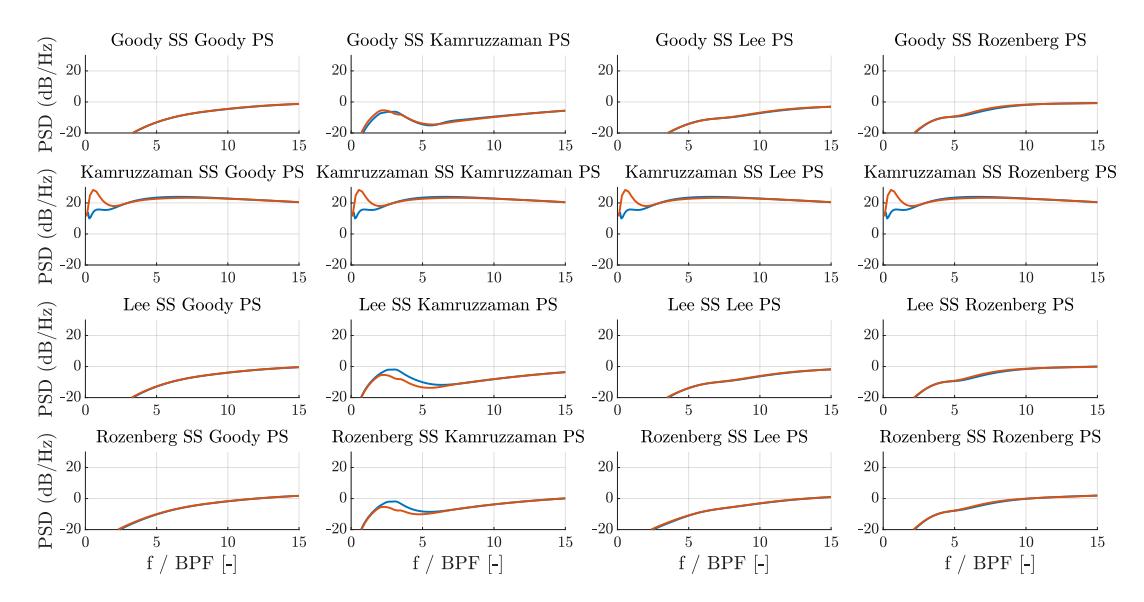


Figure 5.22: Comparison of the trailing edge noise emission on the rotation axis with other WPF functions. Red lines for Middle propeller and blue lines for the isolated one.

Chapter 6

Conclusion and Future Works

This chapter discusses the main conclusions of the work carried out, along with possible directions for future developments.

6.1 Conclusion

The first goal was to assess the capability of FLOWUnsteady in predicting aero-dynamic quantities in specific test cases. The single-propeller configuration was investigated in this work (as well as in others), and the results confirm that FLOWUnsteady provides accurate predictions, in many cases comparable with experimental and VLES data. The solver achieves good convergence at a relatively low computational cost, with only minor discrepancies with respect to high-fidelity methods. Similar behavior is observed for the distributed configuration. For both cases, the main difficulty was related to the tuning of the hub—tip correction parameters, but accurate results were obtained nonetheless. These discrepancies could likely be mitigated by increasing the refinement of the blades and wake.

The second goal was to couple FLOWUnsteady with an in-house aeroacoustic framework. The coupled approach shows good agreement with high-fidelity numerical data, predicting the OASPL with good accuracy. Some discrepancies are visible from the second BPF onwards, likely due to small-scale interactions at the blade tips that are not fully resolved. The directivity is well captured, particularly in the rotor-plane direction, where the sound pressure levels closely match the VLES results. Along the axis of rotation, some discrepancies appear due to an underprediction of the unsteadiness. Broadband noise was analyzed using

different wall-pressure fluctuation (WPF) models: although each led to slightly different sound pressure levels, many provide a good match with the high-fidelity data.

The third objective was to investigate whether the coupled framework can capture the differences between isolated and distributed configurations. FLOWUnsteady successfully reproduced the increase in tonal components along the rotation axis predicted by high-fidelity data. Errors remain small—within the third BPF on the rotor plane and within the first BPF along the axis. The directivity shape shows good agreement with high-fidelity data, with discrepancies along the axis of rotation similar to those already observed in the isolated case. Broadband noise, on the other hand, does not show significant differences between isolated and distributed configurations, in line with high-fidelity predictions.

Overall, the objectives were achieved, and the coupled framework proved to be a reliable tool for predicting both aerodynamic and aeroacoustic performance of distributed configurations in preliminary design stages. It combines low computational cost with good agreement across different noise components when compared to high-fidelity methods.

6.2 Future Work

To further improve the reliability and applicability of the coupled framework, several developments are recommended:

- The integration of a panel method into FLOWUnsteady to account for the aerodynamic and aeroacoustic interactions with non-lifting surfaces such as fuselages and nacelles.
- The definition of clear criteria for setting the FLOWUnsteady parameters such as the hub-tip correction. Possible approaches include the use of machine learning algorithms or the creation of a dedicated database.
- The enhancement of the aeroacoustic framework by reducing the simplifying assumptions currently adopted. In particular, the implementation of subroutines capable of handling generic bodies such as wings, fuselages, and nacelles would increase its generality.
- A more detailed investigation of the influence of resolution parameters on the solution is required.

Appendix A

Wall Pressure Function

The models behind the wall pressure spectra used in this work are described here. The chapter is based on Reference [27].

A.1 Goody

The Goody's model was developed by fitting the experimental results in zero pressure gradient flow. It correctly scales with the middle and high frequencies, and it was demonstrated that it is the most accurate for zero pressure gradient flow [33].

Table A.1: Parameters of the Goody Model.

Parameter	Value / Definition
\overline{a}	3
b	2
c	0.75
d	0.5
e	3.7
f	1.1
g	-0.57
h	7
i	1
SS	$rac{U_e}{ au_w^2\delta}$
FS	$rac{\delta}{U_e}$
RT	$\frac{\delta/U_e}{\nu/u_\tau^2}$

A.2 Rozenberg

The Rozenberg's model is an extended version of Goody's model. It takes into account the effects of the adverse pressure gradient also. It must not be used for favorable pressure gradient flows.

Table A.2: Parameters of the Rozenberg Model.

Parameter	Value / Definition
a	$2.82 \Delta^2 \left(6.13 \Delta^{-0.75} + d \right)^e \left(\frac{4.2 \Pi_c}{\Delta} + 1 \right)$
b	2.0
c	0.75
d	$4.76 \left(\frac{1.4}{\Delta}\right)^{0.75} \left[0.375(3.7 + 1.5\beta_c) - 1\right]$
e	$3.7 + 1.5\beta_c$
f	8.8
g	-0.57
h	$\min\left(3, \frac{19}{\sqrt{RT}} + 4\right)$
i	4.76
SS	$rac{U_e}{ au_w^2\delta^*}$
FS	$rac{\delta^*}{U_e}$
RT	$\frac{\delta/U_e}{\nu/u_\tau^2}$

A.3 Kamruzzaman

The Kamruzzaman's model is well suited for highly loaded boundary layers. Its coefficients are derived from measurements on airfoils at different angles of attack and Reynolds numbers.

Table A.3: Parameters of the Kamruzzaman Model.

Parameter	Value / Definition
a	$0.45 \left[1.75 \left(\Pi_c^2 \beta_c^2 \right)^m + 15 \right]$
b	2
c	1.637
d	0.27
e	2.47
f	1.15
g	$-\frac{2}{7}$
h	7
i	1
SS	$rac{U_e}{ au_w^2\delta^*}$
FS	$rac{\delta^*}{U_e}$
RT	$\frac{\delta^*/U_e}{\nu/u_\tau^2}$

A.4 Catlett

The Catelett's model is another extension of the Goody's model for adverse pressure gradient flows.

Table A.4: Parameters of the Catlett Model.

Parameter	Value / Definition
\overline{a}	$3 + \exp\left[7.98(\beta_{\Delta^*} Re_{\Delta^*}^{0.35})^{0.131} - 10.7\right]$
b	2
c	$0.912 + 20.9(\beta_{\delta}Re_{\delta}^{0.05})^{2.76}$
d	$0.397 + 0.328(\beta_{\Delta^*} Re_{\Delta^*}^{0.35})^{0.31}$
e	$3.872 - 1.93(\beta_{\delta}Re_{\delta}^{0.05})^{0.628}$
f	$2.19 - 2.57(\beta_{\delta}Re_{\delta}^{0.05})^{0.224}$
g	$-0.5424 + 38.1(\beta_{\delta}H^{-0.5})^{2.11}$
h	$7.31 + 0.797(\beta_{\Delta^*} Re_{\Delta^*}^{0.35})^{0.0724}$
i	1
SS	$rac{U_e}{ au_w^2\delta}$
FS	$rac{\delta}{U_e}$
RT	$\frac{\delta/U_e}{\nu/u_\tau^2}$

A.5 Hu

The Hu's model is developed for both adverse pressure gradient and favorable pressure gradient flows.

Table A.5: Parameters of the Hu Model.

Parameter	Value / Definition
\overline{a}	$\left(81.004 \cdot 10^{-5.8 \cdot 10^{-5} Re_{\theta} H - 0.35} + 2.154\right) 10^{-7}$
b	1
\mathcal{C}	$1.5 \left(1.169 \ln H + 0.642\right)^{1.6}$
d	$10^{-5.8 \cdot 10^{-5} Re_{\theta} H - 0.35}$
e	$\frac{1.13}{\left(1.169\ln H + 0.642\right)^{0.6}}$
f	7.645
g	-0.411
h	6
i	1
SS	$rac{u_{ au}}{q^2 heta}$
FS	$rac{ heta}{U_e}$
RT	$\frac{u_{\tau}\delta}{\nu}$

A.6 Lee

Lee's model was developed by observing the trends and limitations of the other wall pressure functions exposed. This model works for zero pressure gradient and relatively low favorable pressure gradient. It is an extension of Rozenberg's model.

Table A.6: Parameters of the Lee Model.

Parameter	Value / Definition
a	$\max(a_{\text{Roz}}, (0.25\beta_c - 0.52) a_{\text{Roz}})$
b	2
c	0.75
d	$\begin{cases} \max(1, 1.5d_{\text{Roz}}), & \beta_c < 0.5 \\ d_{\text{Roz}}, & \beta_c \ge 0.5 \end{cases}$
e	$3.7 + 1.5\beta_c$
f	8.8
g	-0.57
h	$\min(3, 0.139 + 3.1043\beta_c) + 7$
i	4.76
SS	$rac{U_e}{ au_w^2 \delta^*}$
FS	$rac{\delta^*}{U_e}$
RT	$\frac{\delta/U_e}{\nu/u_\tau^2}$

Appendix B

Radiation Integral

B.1 Terms of Radiation Integral

In this section, the coefficients for the radiation integral are presented.

$$S_0^2 = x_1^2 + \beta^2(x_2^2 + x_3^2)$$

$$E^*(x) = \int_0^x \frac{e^{-it}}{\sqrt{2\pi t}} dt = C_2(x) - iS_2(x)$$

$$\Phi^{\circ}(Z) = \frac{1}{\sqrt{\pi}} \int_0^{Z^2} \frac{e^{-z}}{\sqrt{z}} \,\mathrm{d}z$$

$$k = \frac{\omega}{c_0} = \frac{K}{M}$$

$$\beta^2 = 1 - M^2$$

$$K = \frac{\omega}{U}$$

$$\bar{K} = Kb$$

$$\bar{\mu} = \frac{\bar{K}M}{\beta^2}$$

B.1.1 Supercritical gust

$$B = \bar{K}_1 + M\bar{\mu} + \bar{\kappa},$$

$$\bar{\kappa}^2 = \bar{\mu}^2 - \frac{\bar{K}_2^2}{\beta^2}$$

$$\Theta = \sqrt{\frac{\bar{K}_1 + \bar{\mu}M + \bar{\kappa}}{\bar{K} + \bar{\mu}M + \bar{\kappa}}}$$

$$H = \frac{(1+i)e^{-4i\bar{\kappa}}(1-\Theta^2)}{2\sqrt{\pi}(\alpha-1)\bar{K}\sqrt{B}}$$

$$D = \bar{\kappa} - \bar{\mu} \frac{x_1}{S_0}$$

$$G = (1+\varepsilon)e^{i(2\bar{\kappa}+D)}\frac{\sin(D-2\bar{\kappa})}{D-2\bar{\kappa}} + (1-\varepsilon)e^{i(-2\bar{\kappa}+D)}\frac{\sin(D+2\bar{\kappa})}{D+2\bar{\kappa}}$$
$$+ \frac{(1+\varepsilon)(1-i)}{2(D-2\bar{\kappa})}e^{4i\bar{\kappa}}E^*(4\bar{\kappa}) - \frac{(1-\varepsilon)(1+i)}{2(D+2\bar{\kappa})}e^{-4i\bar{\kappa}}E(4\bar{\kappa})$$
$$+ \frac{e^{2iD}}{2}\sqrt{\frac{2\bar{\kappa}}{D}}E^*(2D)\left[\frac{(1+i)(1-\varepsilon)}{D+2\bar{\kappa}} - \frac{(1-i)(1+\varepsilon)}{D-2\bar{\kappa}}\right]$$

$$C = \bar{K}_1 - \bar{\kappa} \left(\frac{x_1}{S_0} - M \right)$$

B.1.2 Subcritical gust

$$\bar{k}' = \sqrt{\left(\frac{\bar{K}_2}{\beta} - \bar{\mu}^2\right)}$$

$$C = \bar{K}_1 - \bar{k}' \left(\frac{x_1}{S_0} - M \right)$$

$$A' = \bar{K} + M\bar{\mu} - i\bar{k}'$$

$$A_1' = \bar{K_1}' + M\bar{\mu} - i\bar{k}'$$

$$\Theta' = \sqrt{\frac{A_1'}{A'}}$$

$$H'\frac{(1+i)(1-\Theta'^2)}{2\sqrt{\pi}(\alpha-1)\bar{K}\sqrt{A_1'}}$$

Bibliography

- [1] Advisory Council for Aviation Research and Innovation in Europe (ACARE), Fly the green deal: Europe's vision for sustainable aviation, Manuscript completed in June 2022, 2022. DOI: 10.2777/732726. [Online]. Available: https://www.acare4europe.org/wp-content/uploads/2022/06/20220815_Fly-the-green-deal_LR-1.pdf.
- [2] F. Galante, «Numerical aerodynamic investigation of two propellers in side-by-side configuration», Supervisors: Francesco Avallone, Renzo Arina, Christophe Schram, Alessandro Zarri, Julien Christophe, Marco Picillo, Master's thesis, Politecnico di Torino and von Karman Institute for Fluid Dynamics, Turin, Italy and Rhode-Saint-Genèse, Belgium, 2024.
- [3] H. D. Kim, A. T. Perry, and P. J. Ansell, «A review of distributed electric propulsion concepts for air vehicle technology», in AIAA Propulsion and Energy Forum, 2018 AIAA/IEEE Electric Aircraft Technologies Symposium, Cincinnati, Ohio: American Institute of Aeronautics and Astronautics, Jul. 2018. DOI: 10.2514/6.2018-4998.
- [4] sUAS News. «Vahana has come to an end. but a new chapter at airbus has just begun». Accessed on October 7, 2025. (2019), [Online]. Available: https://www.suasnews.com/2019/12/vahana-has-come-to-an-end-but-a-new-chapter-at-airbus-has-just-begun/.
- [5] P. A. Koutsoukos, «Aerodynamic and aeroacoustic interaction effects of a distributed-propeller configuration in forward flight: A computational investigation», Defended publicly on January 20, 2022, Master's thesis, Delft University of Technology, 2022. [Online]. Available: http://repository.tudelft.nl/.
- [6] J. Goyal, T. Sinnige, F. Avallone, and C. Ferreira, «Benchmarking of aerodynamic models for isolated propellers operating at positive and negative thrust», *AIAA Journal*, 2022. DOI: 10.2514/1.J064093. [Online]. Available: https://doi.org/10.2514/1.J064093.

- [7] J. Goyal, «Aerodynamics and aeroacoustics of propeller operation at negative thrust: A computational study», Final published version, Dissertation, Delft University of Technology, 2025. DOI: 10.4233/uuid:0cf573ad-f7ca-41d6-8b43-342359f50db6. [Online]. Available: https://doi.org/10.4233/uuid:0cf573ad-f7ca-41d6-8b43-342359f50db6.
- [8] E. J. Alvarez, «Reformulated vortex particle method and meshless large eddy simulation of multirotor aircraft», Theses and Dissertations. 9589, PhD Thesis, Brigham Young University, Jun. 2022. [Online]. Available: https://scholarsarchive.byu.edu/etd/9589.
- [9] A. Zarri, A. Koutsoukos, F. Avallone, F. de Prenter, D. Ragni, and D. Casalino, «Aeroacoustic interaction effects of adjacent propellers in forward flight», in AIAA AVIATION 2023 Forum, San Diego, CA, USA, 2023. DOI: 10.2514/6. 2023-4459.
- [10] Delft University of Technology. «Propeller models flight performance / propulsion / propeller aerodynamics / facilities». Accessed on October 7, 2025. (n.d.), [Online]. Available: https://www.tudelft.nl/lr/organisatie/afdelingen/flow-physics-and-technology/flight-performance-propulsion/flight-performance/propeller-aerodynamics/facilities/propeller-models.
- [11] T. C. A. Stokkermans, «Aerodynamics of propellers in interaction dominated flowfields: An application to novel aerospace vehicles», Dissertation (TU Delft), Delft University of Technology, 2020. DOI: 10.4233/uuid:46178824-bb80-4247-83f1-dc8a9ca7d8e3. [Online]. Available: https://doi.org/10.4233/uuid:46178824-bb80-4247-83f1-dc8a9ca7d8e3.
- [12] G. S. Winckelmans, «Topics in vortex methods for the computation of threeand two-dimensional incompressible unsteady flows», Submitted February 24, 1989, Ph.D. dissertation, California Institute of Technology, Pasadena, California, Feb. 1989.
- [13] L. F. da Conceição Vargas, «Wind turbine noise prediction: Previsão de ruído em turbinas eólicas», Master's Thesis, Instituto Superior Técnico, Universidade Técnica de Lisboa, Lisboa, Nov. 2008.
- [14] P. Singh, "Aeromechanics of coaxial rotor helicopters using the viscous vortex particle method", Doctoral Committee: Peretz P. Friedmann (Chair), Carlos E. S. Cesnik, Bogdan I. Epureanu, Krzysztof J. Fidkowski, Ph.D. dissertation, University of Michigan, Ann Arbor, MI, USA, 2020.

- [15] E. Alvarez, J. Mehr, and A. Ning, «FLOWUnsteady: An Interactional Aerodynamics Solver for Multirotor Aircraft and Wind Energy», in *AIAA Aviation Forum*, Manuscript accompanying the presentation delivered at AIAA AVIATION Forum 2022, AIAA, Chicago, IL, United States, 2022. [Online]. Available: https://scholarsarchive.byu.edu/facpub/5830.
- [16] E. J. Alvarez and A. Ning, «Reviving the vortex particle method: A stable formulation for meshless large eddy simulation», arXiv preprint arXiv:2206.03658, Jun. 2022, Preprint, submitted for publication on December 2021. [Online]. Available: https://arxiv.org/abs/2206.03658.
- [17] T. Berdowski, «3d lagrangian vpm-fmm for modelling the near-wake of a hawt: The development of a stable, accurate, and efficient numerical solver for large-scale wind energy purposes», Presented on May 07, 2015, Master's Thesis, Delft University of Technology, May 2015.
- [18] M. Drela, «XFOIL: An Analysis and Design System for Low Reynolds Number Airfoils», in Low Reynolds Number Aerodynamics, T. J. Mueller, Ed., Berlin, Heidelberg: Springer Berlin Heidelberg, 1989, pp. 1–12, ISBN: 978-3-642-84010-4. DOI: 10.1007/978-3-642-84010-4 1.
- [19] L. A. Viterna and D. C. Janetzke, «Theoretical and experimental power from large horizontal-axis wind turbines», National Aeronautics and Space Administration, Lewis Research Center, Cleveland, Ohio, Technical Report NASA-TM-82944, Sep. 1982, Prepared for U.S. Department of Energy, Conservation and Renewable Energy, Wind Energy Technology Division. DOI: 10.2172/6703041. [Online]. Available: https://www.osti.gov/servlets/purl/6763041/.
- [20] S. A. Ning, «A simple solution method for the blade element momentum equations with guaranteed convergence», *Wind Energy*, vol. 17, no. 9, pp. 1327–1345, 2014. DOI: 10.1002/we.1636.
- [21] E. J. Alvarez and A. Ning, «High-fidelity modeling of multirotor aerodynamic interactions for aircraft design», AIAA Journal, Aug. 2020. DOI: 10.2514/1. J059178.
- [22] F. A. Everest and K. C. Pohlmann, Master Handbook of Acoustics, 5th. New York: McGraw-Hill Education, 2015, ISBN: 9780071841047.
- [23] S. Glegg and W. Devenport, Aeroacoustics of Low Mach Number Flows: Fundamentals, Analysis, and Measurement, 1st. London: Academic Press, 2017, ISBN: 978-0-12-809651-2.
- [24] U. Author, «Aeroacoustics of flight vehicles: Theory and practice. volume 1: Noise sources», NASA, Washington, DC, NASA Reference Publication 1258, Vol. 1; WRDC Technical Report 90-3052, Aug. 1991, Unclassified, p. 601.

- [25] M. Picillo, F. Avallone, et al., «Mid-fidelity framework for rotor noise prediction in maneuvering flight», in *Proceedings of [Conference name]*, Conference Paper, Jun. 2025. [Online]. Available: https://www.researchgate.net/publication/393231020.
- [26] F. Bellelli, R. Arina, F. Avallone, and S. Moreau, «Analytical model for predicting rotor-stator interaction tonal noise in low-speed axial fans», *Dipartimento di Ingegneria Meccanica ed Aerospaziale, Politecnico di Torino*, 2024, Manuscript submitted for publication.
- [27] S. Lee, L. Ayton, F. Bertagnolio, S. Moreau, T. P. Chong, and P. Joseph, «Turbulent boundary layer trailing-edge noise: Theory, computation, experiment, and application», *Progress in Aerospace Sciences*, vol. 126, p. 100737, 2021. DOI: https://doi.org/10.1016/j.paerosci.2021.100737.
- [28] M. Roger and S. Moreau, «Back-scattering correction and further extensions of amiet's trailing-edge noise model. part 1: Theory», *Journal of Sound and Vibration*, vol. 286, no. 3, pp. 477–506, 2005. DOI: 10.1016/j.jsv.2004.10.054.
- [29] J. Goyal, Blade element momentum theory for positive and negative thrust propellers, 2023. [Online]. Available: https://doi.org/10.4121/e748a68d-5f15-4757-b904-880bcec8217b.
- [30] R. de Vries, N. van Arnhem, T. Sinnige, R. Vos, and L. L. Veldhuis, «Aerodynamic interaction between propellers of a distributed-propulsion system in forward flight», *Aerospace Science and Technology*, vol. 118, p. 107 009, 2021. DOI: 10.1016/j.ast.2021.107009.
- [31] M. E. Goldstein, *Aeroacoustics*. New York: McGraw-Hill International Book Company, 1976.
- [32] E. Alvarez, A. Schenk, T. Critchfield, and A. Ning, «Rotor-on-rotor aeroacoustic interactions of multirotor in hover», *Journal of the American Helicopter Society*, 2020, (in review). [Online]. Available: https://scholarsarchive.byu.edu/facpub/4053.
- [33] Y. F. Hwang, W. K. Bonness, and A. Hambric, «Comparisons of semi-empirical models for turbulent boundary layer wall pressure spectra», *J. Sound Vib.*, vol. 319, pp. 199–217, 2009. DOI: 10.1016/j.jsv.2008.06.003.